INSTITUTO SUPERIOR TÉCNICO
Universidade Técnica de Lisboa

# Preliminary Biomechanical Studies on the Diaphragmatic Function in Control and Patients with Loss of Motor Units

**Nuno José Gomes dos Santos**

Dissertation for obtaining the Master's Degree in

## Biomedical Engineering

**Jury**

| | |
|---|---|
| President: | Prof. Hélder Carriço Rodrigues |
| Supervisors: | Prof. Eduardo Borges Pires (IST) |
| | Prof. Mamede de Carvalho (FML) |
| Member: | Prof. Fernando Manuel Fernandes Simões |

**November 27, 2009**

# Acknowledgments

First of all I want to thank my mom, dad and sis for all the support and patience demonstrated during these past months. Every time I had a moment of difficulty they supported me with all the love they could give and with some words of incentive. I know that sometimes during the thesis I was a little bit annoying and stressing but they showed me their untiring compassion and understanding just by smiling to me.

My closest friends were curious about the work I was doing and they showed interest in its subject. I was very pleased with all the questions they made. They helped me to question myself about some issues and learn more about the subject of the thesis. They also helped me to relax with several moments of fun and joy during these past months.

I want also to thank my supervisors who supported the work and effort I had and helped me to surpass all the problems and doubts during the preparation of this work.

The doctoral students Matilde Pato and Daniel Lopes were of a special support in some of my decisions during the thesis. I want to thank them for the availability shown every time I asked for their help.

I want to give a special thank to Cecília Monteiro M.D. and to Nuno Abecassis M.D. and the rest of the medical professionals of the second floor of the surgery room of the *Instituto Português de Oncologia* who gently allowed me to attend two pulmonary surgeries. Both of these surgeries helped me to learn more about the anatomy of the diaphragm.

# Abstract

The main objectives of this thesis are the construction of a three-dimensional (3D) model of the diaphragm and the simulation of the movement of this organ during breathing in normal and pathological cases. The 3D reconstruction of the diaphragm is obtained from segmented images of axial and sagittal views of sectional cuts of a female diaphragm. The finite element analyses of the model are performed during quiet breathing considering three different conditions: a normal diaphragm, a dysfunctional diaphragm caused by amyotrophic lateral sclerosis (ALS) and a diaphragm with a right inactivated hemidiaphragm caused by an unilateral lesion of the phrenic nerve.

Values of the tidal volume and of the maximum axial displacement of the diaphragm are obtained during quiet breathing in all three situations. In the pathological cases these values are significantly smaller than in the normal case, but the volume in the case of ALS patients is larger than in the other pathological case. Thus the impact of the complete right phrenic nerve lesion on the volume is greater than in the ALS case for the same amount of loss of motor units. This suggests that the inspiratory muscles of a patient with such lesion become more activated due to a compensatory response.

# Keywords

Diaphragm, 3D Reconstruction, Finite Element Model, Hill's Muscle Model, Amyotrophic Lateral Sclerosis, Unilateral Lesion of the Phrenic Nerve.

# Resumo

O objectivo principal desta tese é a construção de um modelo tridimensional (3D) do diafragma e a simulação do movimento deste órgão num caso saudável e em dois casos patológicos, durante um ciclo respiratório. A reconstrução 3D do diafragma é obtida a partir da segmentação de imagens axiais e sagitais de um diafragma feminino. As análises por elementos finitos são realizadas no modelo do diafragma durante uma respiração em repouso, considerando três condições: um diafragma são, um diafragma com uma disfunção causada por esclerose lateral amiotrófica (ALS) e um diafragma com o seu lado direito inactivo devido a lesão unilateral do nervo frénico.

Obtiveram-se valores para o volume corrente e para o deslocamento axial máximo do diafragma no caso de uma respiração em repouso. Nos casos patológicos estes mesmos valores são significativamente mais baixos do que no caso normal. No entanto o volume corrente no caso de um doente com ALS é superior ao volume corrente obtido através de um diafragma inactivo num dos lados. Este resultado sugere que os músculos inspiratórios dos doentes com lesão unilateral do nervo frénico possam desenvolver uma resposta compensatória devido à inactivação das fibras do hemidiafragma direito.

# Palavras Chave

Diafragma, Reconstrução 3D, Modelo de Elementos Finitos, Modelo Muscular de Hill, Esclerose Lateral Amiotrófica, Lesão Unilateral do Nervo Frénico.

# Contents

# List of Figures

# List of Tables

# List of Abbreviations [1]

| | | | |
|---|---|---|---|
| ALS | Amyotrophic Lateral Sclerosis | - | Esclerose Lateral Amiotrófica |
| ATP | Adenosine TriPhosphate | - | Adenosina TriFosfato |
| CT | Computed Tomography | - | Tomografia Computorizada |
| d.o.f. | degrees of freedom | - | graus de liberdade |
| EMG | Electromyography | - | Electromiografia |
| FEM | Finite Element Method | - | Método de Elementos Finitos |
| FRC | Functional Residual Capacity | - | Capacidade Residual Funcional |
| MAD | Maximum Axial Displacement | - | Deslocamento Axial Máximo |
| MCAT | Mathematical CArdiac Torso | | |
| MRI | Magnetic Resonance Imaging | - | Imagiologia de Ressonância Magnética |
| NLM | National Library of Medicine | - | Biblioteca Nacional de Medicina |
| NURBS | Non-Uniform Rational B-Spline | | |
| Pdi | Transdiaphragmatic Pressure | - | Pressão Transdiafragmática |
| PMHS | Post-Mortem Human Subject | - | Cadáver |
| REM | Rapid Eye Movement | - | Movimento Rápido dos Olhos |
| SPECT | Single Photon Emission Computed Tomography | - | Tomografia Computorizada por Emissão de Fotão Único |
| TLC | Total Lung Capacity | - | Capacidade Pulmonar Total |
| TV | Tidal Volume | - | Volume Tidal |
| US | Ultrasound | - | Ultrasom |
| VHP | Visible Human Project | | |

[1] Note: This list is in alphabetic order

# List of Symbols

| | |
|---|---|
| $\boldsymbol{\sigma}$ | Cauchy Stress Tensor |
| $\mathbf{F}$ | Deformation Gradient |
| $\mathbf{B}$ | Left Cauchy-Green Strain Tensor |
| $\mathbf{C}$ | Right Cauchy-Green Strain Tensor |
| $I_1^C$ | First Invariant of the Right Cauchy Green Tensor |
| $\mathbf{I}$ | Identity Tensor |
| $\lambda_f$ | Stretch Ratio of the Muscle Fibres |
| $\mathbf{N}$ | Direction of the Muscle Fibres in the Undeformed Configuration |
| $\mathbf{n}$ | Direction of the Muscle Fibres in the Deformed Configuration |
| $T$ | Nominal Stress in the fibre |
| $U$ | Strain Energy |
| $\alpha(t)$ | Activation Function |
| $\alpha_{min}$ | Minimum Value of the Activation |
| $u(t)$ | Neural Excitation |
| $u_{max}$ | Value of the Excitation applied during Inspiration |
| $\tau_{rise}$ | Time Constant for the Activation of the Muscle |
| $\tau_{fall}$ | Time Constant for the Deactivation of the Muscle |
| $a$ | Material Parameter |
| $b$ | Material Parameter |
| $c$ | Material Parameter |
| $A$ | Material Parameter |
| $T_0$ | Maximum Tensile Stress |
| $p$ | Hydrostatic Pressure |

# 1

# Introduction

## Contents

## 1.1 Context

The diaphragm is considered the main respiratory muscle responsible for maintaining the correct change in pulmonary volume at the inspiration step of the respiratory cycle. For this reason the diaphragm plays an important role in human life because respiration is an indispensable and vital aspect of the human body system.

Despite the differences between animals, all of them have the basic necessity of breathing as a common process of acquisition of oxygen and removal of carbon dioxide from the system. All animals require energy to sustain their body activities and perform their own actions. The energy is collected in the last step of the metabolism in the form of ATP molecules obtained by a chain of reactions where the oxygen is consumed and water and carbon dioxide are formed. Both respiratory and cardiovascular systems have then the responsibility to carry the oxygen into the cells and to carry out efficiently the carbon dioxide from the cells.

The exchange of oxygen and carbon dioxide between the outside air and the body is done in different ways with different methods in different animals. In humans this procedure has three main steps from the outside to the cells. The oxygen enters the body mixed in the air by the mouth or the nose and fills the lungs. At this moment, oxygen and carbon dioxide are exchanged; oxygen enters the blood stream while carbon dioxide is released into the lungs and then expelled. Oxygen is then delivered to the cells where is once more exchanged with carbon dioxide; the latter passes to the blood stream while the oxygen enters the cells.

In all the steps of this path, from the outside to the cells, different body systems intervene. It is therefore important to maintain the homoeostasis of those systems. However this condition is sometimes compromised leading to a pathological disease. For this reason it is important to perform tests for a correct diagnosis, but because of the large number of possible diagnoses, physicians have to decide which test is the most adequate to perform. After this it is necessary to consider a treatment which varies depending on the nature of the pathology.

With respect to this issue, there is, therefore, the need to create and develop tools able to predict in an approximated range some biological and mechanical behaviours. Then physicians would be able to obtain a more accurate and earlier diagnosis which is very important for a more correct treatment. In some pathologies the earlier the disease is diagnosed the better will be the final result of the treatment. Focusing at this problem and solution, the main goal of this thesis is a step in the achievement of a computational tool and its application to clinical cases.

Mechanically, respiration is a cycling process of muscle contractions that help the air to periodically enter and leave the lungs. In this manner diaphragm is one of the ventilatory muscles responsible to actively expand the lungs downward. Other muscles are classified as inspiratory muscles, however the diaphragm has the highest contribution to the total work performed by all muscles (about 60 to 80% [9]). This is the main reason why to perform a study on this muscle.

One of the pathologies characterized and studied in this work is amyotrophic lateral sclerosis (ALS). ALS is a neurodegenerative disease of the upper and lower motor neurons resulting in muscular atrophy and spasticity [10]. Although all muscles are affected by this pathology, respiratory muscles are the most concerned. Most patients with ALS (incidence from 1 to 3 per 100,000 and prevalence ranging from 4 to 8 per 100,000 [10]) die from respiratory complications. ALS is a progressive, fatal illness with a mean survival from time of diagnosis of only 1 to 5 years, although 5 to 10% of patients survive for more than 10 years.

There are other causes of diaphragm paresis, namely those derived from phrenic nerve injury. The central nervous system and the diaphragm are connected by the phrenic nerve. Each half of the diaphragm is innervated by the right and the left phrenic nerves. When the phrenic nerve is injured, as a consequence of a surgical intervention or of an inflammatory process, the diaphragm paralyses. When of one of the phrenic nerves is denervated the paralysis is unilateral.

The main objective of this work is to simulate computationally the mechanical behaviour of the diaphragm in healthy and pathological conditions. To complete this objective it is necessary to first obtain a three-dimensional geometric model of the diaphragm from medical images taken from a cadaver. The subsequent mechanical modelling and the choice of good parameters are important to obtain reliable numerical simulations.

The Finite Element Method (FEM) is used in this study to perform the numerical simulations. FEM is a numerical technique for finding approximate solutions for boundary value problems encountered in engineering and science. The corresponding governing equations are approximated by a system of algebraic equations which has to be numerically stable to avoid the accumulation of errors during the analysis and obtain results with mechanical meaning. The FEM is a good tool to solve partial differential equations over complex domains.

Nowadays the FEM is a technique used in a wide range of applications in all kind of scientific areas. The FEM is useful in structural, thermal, electromagnetic and fluids problems. In biomedical engineering the FEM analysis is also performed currently. It allows the simulation of very different biological processes and situations in the human body.

In order to obtain a finite element mesh, a geometric model of the bodies under study is needed. The model reconstruction is the process of computationally representing a three-dimensional object. The existing methods used to model an object are not very robust because they need various previous assumptions. Almost all of them are user dependent. There are also semi-automatic and automatic techniques but they are very limited. The geometrical reconstruction of objects is required in many applications concerned with modelling, simulation, visualization and FEM analysis. Its importance and relevance is enormous because very realistic models are created which allow the analysis of real situations. The scientific areas that need reconstruction of objects are also diverse.

In biomedical engineering the model reconstruction is essentially used to visualization and

FEM analysis. The human body anatomy and systems are very complex and their reconstruction is a very difficult task. However if the reconstruction is successfully performed the results will be very useful for subsequent simulations.

## 1.2 Thesis Organization

The thesis is structured as follows. In the next Chapter (2) a brief description of the diaphragm and of the ALS pathology is provided. These two subjects are of extreme importance in this work and therefore the physiological and mechanical properties of the diaphragm and of the ALS disease are referred. In the following Chapter (3) some relevant studies related to the present thesis are mentioned, which are divided in three main parts. The recent and more appropriate studies performed in the 3D reconstruction area are explained and their most important results and conclusions are also referred. In the other section of this Chapter some studies regarding mainly the ALS pathology are mentioned. In Chapter 4 the constitutive model of the diaphragm is introduced. Chapter 5 describes the numerical simulations performed. Basically the practical aspects of this thesis are explained in this Chapter, from the 3D reconstruction to the FEM analyses. In Chapter 6 all the results from the FEM analyses are shown and discussed. In the last Chapter (7) conclusions and future developments are presented.

# 2

# The physiology of the diaphragm

## Contents

Breathing is a natural and vital necessity of the human body. The body system responsible for breathing is the respiratory system consisting of lungs, airways and respiratory muscles. Its main function is to allow gas exchange in the lungs' alveoli by diffusion. The air flows passively in the lungs and airways while that exchange occurs mainly due to the important role played by the muscles. In this manner respiratory muscles, also called ventilation muscles, are the only ones that actively contribute to body breathing. The respiratory system works due to a relationship between its two components, the gas exchanger and its pump.

The respiratory muscles are divided in two groups according to its contribution to respiration. The ones that mainly help the body to inspire are called inspiratory muscles while those helping in expiration are called expiratory muscles. Sternomastoid, external intercostal and diaphragm are inspiratory muscles while rectus abdominis, external and internal oblique and transverse abdominis are expiratory muscles [9]. This work will focus on the diaphragm and for that reason all other muscles will not be described.

## 2.1 Diaphragm

The diaphragm is a musculo-fibrous sheet separating physically and functionally the thorax and the abdomen [11]. It takes the form of the surrounding organs as an elliptical cylindroid capped with a pair of cupolas located on either side of a central plateau. In Figure 2.1, the aspect of a diaphragm is illustrated from both inferior and superior views. In Figure 2.2 a three-dimensional aspect of the diaphragm inserted in the thorax and in the abdominal structures is shown.

At the thoracic part, the diaphragm is surrounded mainly by the lungs and the heart. This outlet is set obliquely to the coronal plane leaving the diaphragm to be superior anteriorly and inferior posteriorly. At the abdominal part, the diaphragm is surrounded mainly by the liver, the spleen, the stomach and the intestine. The presence of the liver in the right side of the body creates a higher cupola relatively to his left cupola, since the liver has an oblique position with respect to the transversal plane.

The diaphragm is attached to and around the abdominal cavity, from the xiphoid process to the vertebrae. Central and anteriorly, the diaphragm is attached by two slips to the back of the xiphoid process, although these slips may be absent. On the opposite side, at the lumbar part, there exist two slices of cartilage in the diaphragm, named crura, which are attached to the first five lumbar vertebrae. Laterally along the costal part, the diaphragmatic muscle is attached to the internal surfaces of the lower six costal cartilages and their adjoining ribs (seventh to twelfth ribs).

The thoracic and abdominal contents determine the shape of the unstressed dome of the diaphragm creating two separate zones: a quasi-horizontal zone, characterized by the two cupolas and the remaining quasi-vertical zone. The former is referred as the diaphragmatic zone while

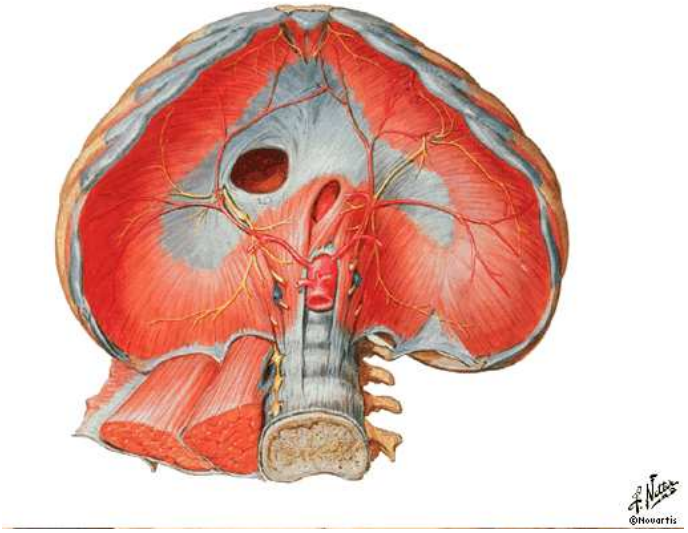


**(a)**

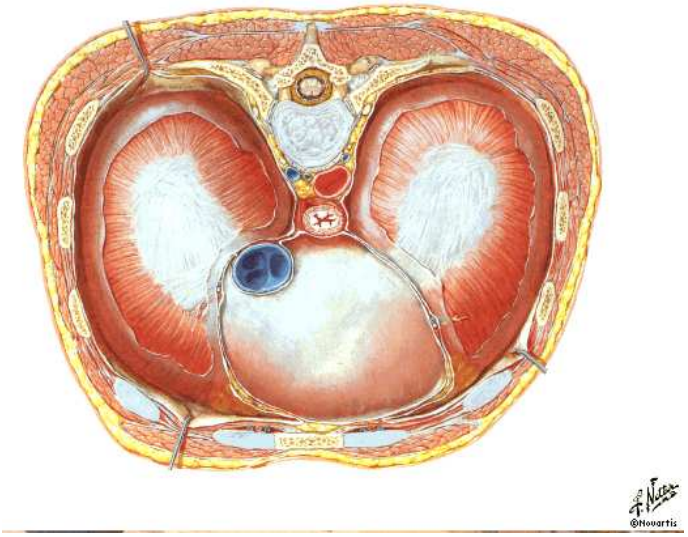


**(b)**

Figure 2.1: Schematic illustration of abdominal (a) and thoracic (b) parts of the diaphragm, inferior to superior and superior to inferior views respectively [1].

Figure 2.2: Three-dimensional aspect of the diaphragm [2].

the latter is referred as the apposition zone (Figure 2.3). The diaphragmatic muscle (without considering the central tendon) is also composed by two main segments: the crural and the costal parts [3]. Crura is essentially located posteriorly starting at the central tendon and descending to attach to the bodies of the first five lumbar vertebrae.

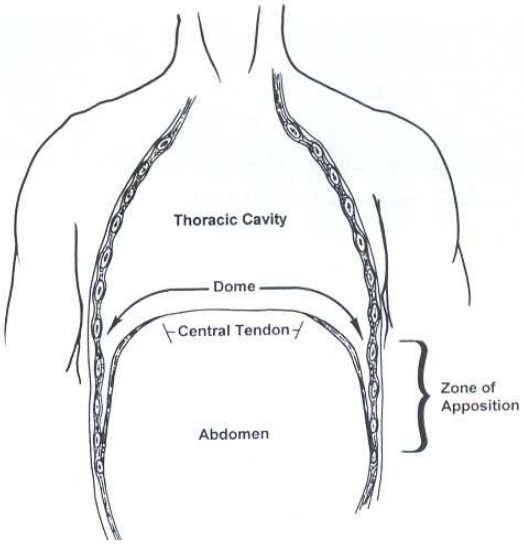


Figure 2.3: Coronal cut of thorax and abdomen *in situ* with a representation of a diaphragm at a functional residual capacity [3].

Like almost every muscle-based organ of the human body, the diaphragm does not only incorporate muscle. In fact, the region at the top of diaphragm is tendon, called the central tendon or the phrenic centre. This sheet is a thin, strong aponeurosis of interwoven collagen fibres, with its anterior margin closer to the front of the diaphragm. This helps the diaphragm to maintain its

shape during contraction. In the extremity of the muscle where the diaphragm is attached to the bones, it is also formed by tendinous tissue. These collagen fibres create a connection between bone and muscle and act as insertions for the muscles.

Since the diaphragm acts like a barrier between thorax to abdominal content it is natural to expect some apertures in the muscle for an up to down communication. Thus blood vessels, oesophagus, nerves and other small structures cross the diaphragm through these openings. Aside small gaps there are three main apertures in the diaphragm. The aortic opening is the most inferior and posterior orifice and, as the name suggests, it is where the aorta artery passes through the diaphragm. This opening lies at the level of the lower border of the twelfth thoracic vertebra and of the thoracolumbar intervertebral disc, slightly to the left of the midline of the body. This is not a true opening because it is not surrounded by diaphragm only. Actually it is a vertical osseo-aponeurotic and symphysio-aponeurotic channel located between the crura laterally, the vertebral column posteriorly and the diaphragm anteriorly.

The oesophageal aperture is elliptical and lies at the level of the tenth thoracic vertebra, with its major axis directed obliquely, almost vertically. It ascends to the left of the midline of the body in the muscular part of the right crus. This aperture allows the passage of the oesophagus, the trunks of the vagus nerves and the oesophageal branches of the left gastric vessels and lymphatic vessels. Although the muscles of the oesophageal wall and of the diaphragm remain separate, there are some elastic fibres from the inferior diaphragmatic fascia that penetrate in the submucosa of the oesophagus. This fascial expansion forms the phreno-oesophageal ligament connecting the oesophagus and the diaphragm in a flexible manner. This allows some freedom of movement during breathing and swallowing.

The cava vein aperture is the highest and largest of the three openings and lies horizontally at the level of the disc between the eighth and the ninth thoracic vertebrae. It has approximately a quadrilateral shape and is located within the central tendon at the junction of its right leaf with the central area. Vena cava passes through this opening and is also adherent to its margin with branches of the right phrenic nerve running laterally with respect to this vein.

Each half of the diaphragm is innervated by the right and left phrenic nerves. The right phrenic nerve reaches the diaphragm just laterally to the inferior vena cava while the left phrenic nerve joins the diaphragm just laterally to the border of the heart. The left phrenic nerve is located in a slightly more anterior plane than the right phrenic nerve. These two branches of the phrenic nerve are subdivided, at the level of the diaphragm or just above it, into several terminal ramifications, the right ones being the mirror of the left ones. This nerve is the only motor supply to the diaphragm and its branches are usually deep within the muscle. However all the crural fibres at the right and left of the oesophageal opening are supplied by the ipsilateral phrenic nerve. These branches act mechanically in a different way from the rest of the diaphragm because of the difference in the nerve supply as suggested in [12].

The contraction of the diaphragm has a specific behaviour according to the respiratory cycle. During inspiration the diaphragmatic muscle shortens actively leading to a decrease in the axial length of its cylindrical portion and consequently the dome descends relative to its costal insertions. On the other hand the zone of apposition will change when the shape of the rib cage changes. When this happens the thoracic cage will expand. During quiet breathing the dome part of the diaphragm does not normally suffer any changes in its shape. After inspiration the muscle returns to its initial position because of its elasticity [2]. This movement is passive contrarily to the inspiration phase. The dome part lifts and the rib cage retrocedes together with the apposition part.

During quiet breathing the decrease in axial length of the apposed diaphragm (essentially the dome part) is about 1 to 3$cm$ [2][11], whereas the increase in the sagittal and coronal diameters of the rib cage is only approximately 0.3 to 0.5$cm$ [11]. Therefore the most important change in the diaphragmatic shape during normal quiet breathing occurs when the fibres in the zone of apposition contract and the dome part of the diaphragm descends. This change is responsible for the major part of the variation in volume. Because of this major axial displacement of its domes, the diaphragm is sometimes referred as a piston-like contractile muscle.

The difference in pressure across the diaphragm is known as transdiaphragmatic pressure (Pdi). It is related to the stresses in the muscle and to the radii of curvature of the diaphragm [13]. Pdi is therefore the total axial force developed by the apposed diaphragmatic fibres divided by their cross-sectional area at the zone of apposition. However, as mentioned before, the shape of the domes does not vary significantly during quiet breathing and therefore the radius of curvature of the diaphragmatic domes also does not need to be considered in assessing the Pdi. This is an advantage because the shape of diaphragm is very complex.

The normal breathing in adult men has a rate of about 18 inspirations per minute during quiet breathing.

## 2.2 Amyotrophic Lateral Sclerosis

Amyotrophic Lateral Sclerosis, also known as Lou Gehrig's disease or Maladie de Charcot, is a progressive neurodegenerative and devastating disorder of the motor cortex, anterior horn cells of the spinal cord and of the motor cranial nuclei that leads to progressive muscle weakness and atrophy [14]. The spinal cord contains the motor neurons witch innervate the limbs and the axial muscles. The anterior horn cells are located in the anterior part of the gray matter as shown in figure 2.4. In this disease the motor neurons degenerate and cease to send messages to the muscles, causing muscle weakness and atrophy.

According to Dangond [14] no cure to this disease is known yet but a number of treatments increases survival and the quality of life.

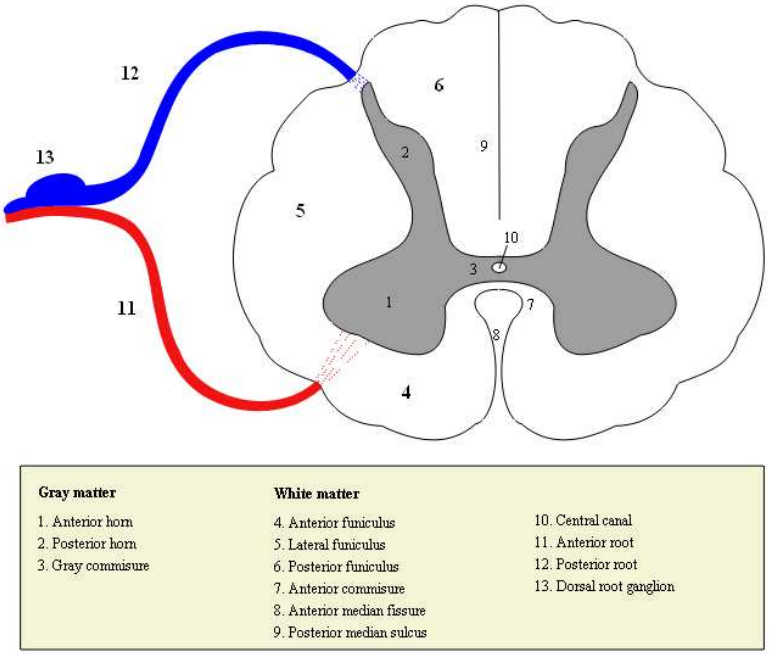


Figure 2.4: Axial section of the spinal cord showing the location of the anterior horn cells.

ALS primarily involves anterior horn cells in the spinal cord and cranial motor nerves. This may lead to progressive bulbar paresis (with inability to control speech, chewing and swallowing). Bulbar-onset is associated with poorer prognosis. Limb weakness is predominantly distal at onset with progressive proximal involvement of the muscles. Spontaneous fasciculations (twitches) and atrophy of the tongue may be noted on physical examination. Brisk deep tendon reflexes, spasticity and extensor plantar reflex represent upper motor neuron lesion. The diaphragm and other respiratory muscles are invariably affected, usually as a late event, and most patients actually die from respiratory failure or respiratory complications [10].

This disease involves both upper and lower motor neurons. Patients develop variable hyperreflexia (condition in which the muscles have an overactive or an over-responsive reflexes due to a bad judge response of the nervous system to a normal stimuli), clonus (a rapid succession of flexions and extensions of a group of muscles), spasticity, extensor plantar responses, limb or tongue fasciculations and Wallerian degeneration of corticospinal and corticobulbar tracts. However the extraocular muscles, bladder and anal sphincter muscles are generally spared. Since only anterior horn cells are affected, sensorial involvement, if any, is minimal. As a consequence of the weakness of the hand muscles, patients may present an inability to write. However gait function may be preserved until later stages.

ALS is a progressive neurodegenerative disease. For this reason it is natural to expect some complications in the patients condition since the appearance of the first symptoms. Therefore ALS can lead to (i) aspiration pneumonia and respiratory insufficiency because of respiratory muscle weakness, (ii) progressive inability to perform activities of daily living such as handling utensils for

self-feeding and dressing up, (iii) deterioration of walking because of lower limb muscles weakness. This last deterioration is the cause for patients to be wheelchair or bedridden dependent. Consequently this situation can originate decubitus ulcers and skin infections because of the resultant patient immobilization.

Most patients with ALS have the sporadic and idiophatic form of this disease. In only 5 to 10% [10][15] of cases, ALS is a familial disorder, usually being transmitted as an autosomal dominant trait. The key mechanisms in both familial and sporadic ALS remain unknown.

After the first symptoms and diagnosis, survival of ALS patients is in a small range of life time. Estimated mean survival from time of diagnosis is only 1 to 5 years [10]. There are some particular patients with familial, juvenile-onset ALS who have been reported to survive for longer periods, about 2 to 3 decades. In all the population, crude mortality rate is about 1 to 3 cases per 100,000 population while in 60 to 75 year-old population the rate rises to approximately 6 cases per 100,000. The worldwide incidence of ALS is about 1 to 3 per 100,000 population [10] while in the United States of America that number rises to approximately 5 cases [14].

ALS has a racial preference to white as compared to non-white people. The white to non-white ratio is about 1.6 to 1. Relatively to sex, ALS affects more males than females in a ratio of a range between 1.5 and 1.6 to 1 [10][14]. Exceptions aside, onset of ALS occurs in the fourth to seventh decades of life being the mean age approximately 66 years.

All of these aspects such as age, race and sex are very important information to be considered and studied because the disease is a complex disorder and is dependent on all of them. They can influence the degeneration of neurons, the rate of weakness and atrophy of muscles, that is, the lifetime of patients and their life's quality.

ALS onset is insidious and this can elude the physicians leading them to other diagnoses. This and other points originate a long delay from onset to diagnosis. The mean duration of this period is about 500 to 680 days.

# 3

# State Of The Art

## Contents

In the last two decades human organs have been the object of relevant biomechanical studies. These studies are very important because they allow a better understanding of the human body, not only medically, but also mechanically. This work tries to study the diaphragm as an active mechanical muscle with physiological properties obtained from the literature.

Behr *et al* [16] performed a study of the diaphragm with the purpose of integrating a geometrical model of the diaphragm in a complete computational model of the human body (the Radioss™ Humos project). Their ultimate goal was to simulate diaphragmatic ruptures involved in road accidents. They reconstructed a 3D geometry of the diaphragm from a post-mortem human subject (PMHS) and assigned mechanical properties to all of its components: the muscular parts, the tendinous parts, the pillars and the different interactions between these parts and the neighbouring organs.

The 3D reconstruction had several steps from the PMHS until its final reconstruction treatment. Firstly the PMHS, an European male, was seated in a car cockpit in a driving position and frozen at -23°$C$ for body conservation. This also facilitated the sectioning of each part of the body. Since the diaphragm is located at the thoracic and abdominal zones, only these regions were considered. These were sliced every 7.5$mm$ with a 2.5$mm$ thick saw and the produced slices were digitized to a standard image format.

The hardest part of the study by Behr *et al* was the identification and contouring of the diaphragm of each slice. It was a non automatic procedure due to the difficulty to identify the contours. At some points an anatomist judgement was also needed for contour adjustment or modification. The last step of the reconstruction consisted of a surface generation based on contours and the consequent necessary improvements, such as smoothing. The surface generation was also not trivial to obtain. They needed to consider an algorithm, the marching cubes algorithm, different from the one used in previous studies. Finally other improvements were performed regarding the hiatus of the inferior vena cava because of its tendinous nature.

In the reconstructed surface different parts were established since the diaphragm has different mechanical properties. For this reason, muscular parts, tendinous parts and pillars were meshed independently. The muscular part was modelled with elastic orthotropic properties and the tendinous part as an elastic isotropic material.

## 3.1 3D Model Reconstruction

The reconstruction of human organs depends on their nature and on the way they are captured. In medical practice there are different techniques to capture human organs for diagnosis. The most reliable procedure is the surgery because organs are visualized directly. However this is an invasive technique not to be performed when only diagnosis is required.

Medical imaging is also an important tool to create images of the human body. Indeed it is

the most important tool used for clinical purposes and medical science. The medical imaging incorporates important techniques used commonly in medicinal practice such as radiography, magnetic resonance imaging, ultrasound and tomography.

These techniques are all different because they use different theoretical approaches for image acquisition. An important consequence is that those procedures are used according to different human organs and diseases. Radiography, for example, is optimal for bone detection but very poor for soft tissue detection. Instead ultrasound is a useful technique for blood vessel detection and its flow.

The diaphragm can also be visualized by some of these techniques.

### 3.1.1 X-ray imaging

Condurache *et al* [4] used X-ray projections to detect and track the diaphragm in a respiratory cycle motion. Although their purpose was not the reconstruction, the diaphragm was detected in X-ray images at different instants of time but with the same view (Figure 3.1). This produced a two-dimensional contour of the diaphragm evolving in time.

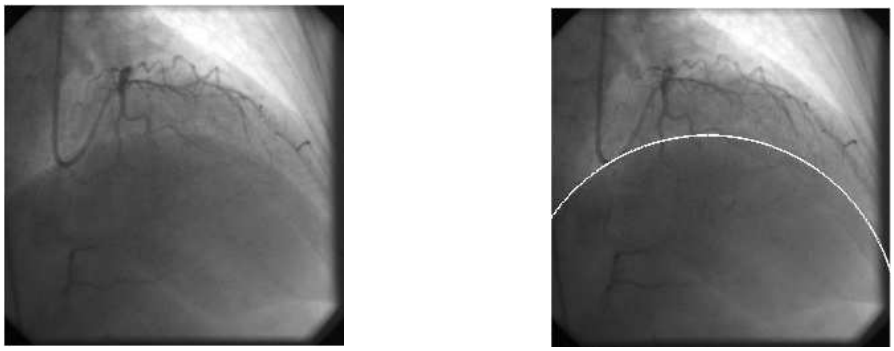

**(a)** **(b)**

Figure 3.1: A cardiac X-ray image (a) and the corresponding diaphragm contour detection (b) [4].

As shown in Figure 3.1, the diaphragm and other neighbouring soft tissues are difficult to distinguish from each other in X-ray based images. However Condurache *et al* successfully obtained the contour of the diaphragm (Figure 3.1(b)) using different algorithms.

First a respiration status was determined since it is necessary to know where the diaphragm is at each time frame. Then the diaphragm was segmented starting from its lateral borders using an algorithm called Hough circular approximation. This algorithm uses edge detection followed by a Hough transform for circles. However another algorithm, the active contour, was still needed in order to correct the diaphragm position when the Hough algorithm failed.

Condurache *et al* concluded that the algorithm is fast and robust and provides good results. However this algorithm is only applicable to two dimensional images of the diaphragm.

### 3.1.2 Photographic imaging

On the other hand Segars *et al* [17] used the mathematical cardiac torso (MCAT) as a model for the upper torso and to simulate the respiratory motion. Indeed the main objective of their study was to remove some artefacts from images of single photon emission computed tomography (SPECT) carried on patients.

In this study Segars *et al* use a different way to model the upper torso, including the diaphragm. They used a 4D Dynamic MCAT phantom modelled by non-uniform rational B-splines (NURBS) and incorporated respiratory motion. NURBS is widely used in 3D computer graphics to describe three-dimensional surfaces because they are represented as a bidirectional parametric object. NURBS surfaces are continuous and therefore they permit representation of a surface with any resolution. Although the mathematical complexities they introduce represent a disadvantage, they allow a vast increase in flexibility to shape more realistic biological models.

The creation of the spline-based MCAT phantom was done considering the Visible Human Project CT data. According to Segars *et al* these spline-based phantoms can model organ shapes and anatomical variations and patient motion more realistically than the simple geometric-based model of the MCAT. The simulation of the respiratory motion was performed by those MCAT phantoms but changing some important parameters in that movement, such as the height of the left and right diaphragm sections and their degree of curvature, and the translation of the heart.

From the results obtained, Segars *et al* concluded that the NURBS surfaces have the potential to model respiratory motion realistically, more than the models based on geometric solids. They also noticed that the volume curve for the right lung of the current MCAT phantom is nearly identical to that of the spline-based phantom.

### 3.1.3 Visible Human Project

The Visible Human Project (VHP) is an effort to create a detailed data set of cross-sectional photographs of the human body in order to facilitate anatomical visualization. The main motivation for the creation of this project resided on the necessity of a library with a complete data set of human organs available online and free. Nowadays this data is available to researchers from academia and industry under a nonfinancial licensing agreement [8].

The data set of VHP corresponds to parts of the entire body of a male and a female cadavers. The cadavers were selected from a group of 3,000 cadavers all around the United States of America [18]. All cadavers were selected through phases according to some requirements, such as absence of anatomical deformation as a result of accidents, diseases or malformations. The history and physical condition of cadavers were taken into account and also some radiographs, computed tomography (CT) and magnetic resonance (MR) images were previously examined by anatomists and physicians.

The selected male donor was a 38 years old Texas man who was executed by lethal injection.

On other hand the selected female cadaver was a 59 years old women from Maryland who died from an heart attack. The male was 1.80m tall and weighted 90.265$kg$ [18] while the female was 1.65m tall and the estimated weight was 124-131$kg$ [19]. As previously referred both specimens had no anatomical deformation. However the male cadaver had only one testicle, his appendix was missing and the tissue at the site of the lethal injection was deteriorated. The female had several pathologies, including cardiovascular disease and her reproductive organs are not representative of those of a young woman because of the age at the time of her death.

The data set of the VHP has a lot of information regarding anatomic visualization. It mainly consists of photographic images of several frontal sections of the entire body of the specimens. Nevertheless there are also radiographies, computed tomographies (CT) and magnetic resonance images (MRI). These images were collected before the photographic images.

After the death of each donor their bodies were carefully prepared to later usage and some procedures were applied to maintain the level of deterioration over time at a minimum. Nevertheless at each step of each procedure, both time and condition of the cadaver were always under continuing monitoring because of the possibility of rapid massive deterioration. This could also explain possible changes in the tissue noticed in later images. After the CT and MR capture in the unfrozen specimens, both cadavers were placed in a plywood mold lined with two layers of plastic. A second CT scan was done to obtain transversal images.

The following procedures were performed to create the sections for later photographic capture. The cadavers were divided in blocks each one representing 1) the head, neck and thorax, 2) legs, ankles and feet, 3) thighs and knees and 4) abdomen and pelvis. Each block was then sectioned along the axial plane by a cryomacrotome blade of 1.3$mm$ thick at each 1.0$mm$ (male) and 0.33$mm$ (female) intervals [8]. The resultant data set is over 15 (male) and 39 Gbytes [8] (female) in size and is available online at the NLM website under a no-cost license agreement. Besides all the information obtained in the VHP the photographic images are the most used amongst all the projects in the science community. Indeed these images are of high quality (captured in 2,048 x 2,048 x 42-bit) and represent the real aspect of human body.

These data sets are being applied to a wide range of educational, diagnostic, treatment planning, virtual reality, artistic, mathematical and industrial uses in more than 27 countries around the globe. In medicine the greatest contributions from VHP consist in providing a complete body of human anatomy, in testing medical imaging algorithms and as a testbed and model for the construction of digital-image libraries. Indeed these libraries are the starting point of a more complex and realistic software where models of body organs can be selected, viewed and even animated (e.g. Voxel-Man 3D-Navigator).

### 3.1.4 Magnetic resonance imaging

Returning to image based reconstruction, Hoyte *et al* [20] have also used magnetic resonance-based images to better identify imaging markers for genuine stress incontinence and pelvic organ prolapse. Indeed they have even compared the structure, volume and integrity of the levator ani muscle between two-dimensional MR images and the consequent reconstructed three-dimensional model.

Hoyte *et al* performed all the reconstruction and used the following procedure. After the acquisition of axial MR images, a radiologist reviewed the source images and measured important parameters for later comparison and confirmation. A gynaecologist performed the manual segmentation of anatomically significant components of the studied region. The three-dimensional surface models were then generated by using a pipeline consisting of dividing cubes, triangle reduction, triangle smoothing and a surface-rendering method called marching cubes.

The marching cubes algorithm [21] is a robust procedure that creates triangle models of constant density surfaces from 3D medical data. Using a divide-to-conquer approach to generate inter-slice connectivity, the algorithm processes the 3D medical data in scan-line order and calculates triangle vertices using linear interpolation. This is a fast algorithm which produces realistic models from three-dimensional data.

From the analysis of the two-dimensional MR images and the three-dimensional models, Hoyte *et al* concluded that the levator ani atrophy and loss of structural integrity are major cofactors in female pelvic floor dysfunction. The study also demonstrates that MR-based 3-D reconstruction is a feasible technique to evaluate the symptomatic female pelvic floor because of the relatively high resolution, the noninvasive nature and the lack of anatomic distortion allowing for the visualization of vital pelvic structures and their study in the physiological state. Nevertheless there were some disagreements between the 2-D and 3-D results because of some variations in the MR slice angle which originated some artefacts both in 2-D images and 3-D models. The authors also noted the lack of surgical or clinical confirmation of their imaging findings as a limitation for their study.

Promayon *et al* [2] studied a 3D functional model of the diaphragm muscle allowing for motion quantifications based on a functional diaphragm representation. They created six models with different purposes: five of these were simplified geometrical models in order to illustrate mechanical aspects of the contraction, to assess the modelling method used and to reproduce the piston motion of the diaphragm, and a sixth model to provide information on both location and motion of the diaphragm.

Promayon *et al* divided their study in two parts, the modelling and the mechanical analysis. The second part will be referred later in this chapter (subsection 3.2.1).

Since the purpose of the study was the functional representation of the diaphragm, the modelling was not as realistic as in the previously mentioned works although the long term goal was the complete physical model and the simulation of its dynamic behaviour. For this reason a

complete reconstruction was made although the resultant models were geometrically simpler but functionally important.

The three-dimensional models obtained in this study are based on MR images. The first step consisted in obtaining the MR images. From four different subjects the images were acquired throughout a respiration cycle. For each subject MRI were also captured at three different levels of current volume (the air volume at the end of inspiration): high volume of 950$cm^3$, basal volume of 480$cm^3$ and an intermediate volume of 720$cm^3$. It is important to notice that this procedure was achieved because the subjects were ventilated passively by a nasal mask. Also this allowed the respiration cycles of each level to be synchronized with each other.

The second step was the post-synchronization. It consisted in choosing the acquired images in a consecutive way at different volumes but corresponding to the same phase of the respiration cycle. This allowed the identification of each image by associating a subject, a volume state and a cycle phase.

The third step was the segmentation. The diaphragm was segmented three times. First the domes were delineated automatically considering the contrast between the lungs (dark in MR images) and the adjacent abdominal organs (lighter in MR images). The zone between the domes was then extrapoled from the extremities of both domes. Finally the apposition zone was also extrapoled in two segments in the delimited region of the abdominal organs and inferior coastal rim.

The last step of the reconstruction was also the first step of the mechanical analysis. Use was made of a physically-based model, *Phymul* [22], to process the reconstruction and also to indicate relevant mechanical properties. *Phymul* is a C++ library which allows the modelling of objects and the simulation of their behaviour in a certain period of time. In Figure 3.2 the six reconstructed models of the diaphragm are displayed. Model A is the geometrically simplest and model F is the most complex. The first two just consider the three axial distances of diaphragm, R, L and A, while the others also incorporate the domes' height, H, and the length of the apposition zone, L. Some other regions (abdominal content, lungs, ribs) are also added to incorporate a realistic behaviour in the interface of the diaphragm.

From a geometrical aspect, Promayon *et al* observed that only the geometric models that incorporated the content under the diaphragm reproduced the same physiological behaviour as *in situ*: decrease of the length of the apposition zone and the lowering of the diaphragmatic domes and abdominal content. Model A demonstrated a chaotic behaviour in the simulations. Model F is the most complex model and Promayon *et al* observed some instabilities in the simulations and therefore suggested some improvements in the modelling such as in the costal cartilage and in some regions of tissue interaction.

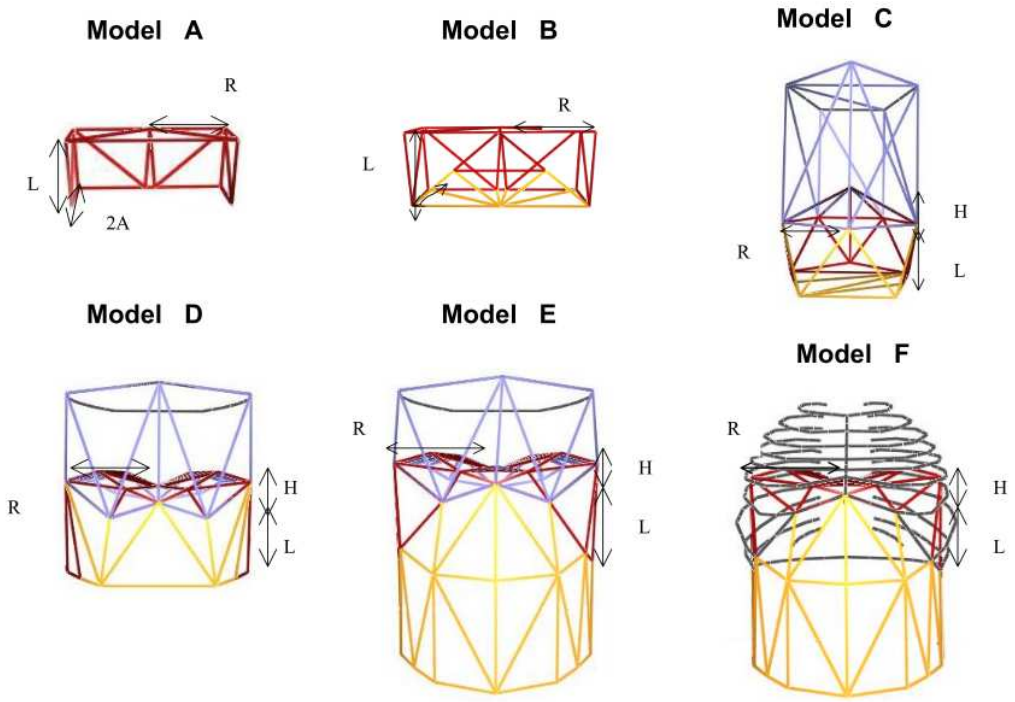


Figure 3.2: Six geometric models of diaphragm: R is the transverse radius of thorax, H is the height of domes, A is the anterior-posterior distance of diaphragm and L is the length of the apposition zone [2].

### 3.1.5 Ultrasound imaging

Quaranta *et al* [5] developed a different method to analyse and model the geometry of the diaphragm. Although MR and CT scans can provide high-quality 3D reconstructions, they present some important limitations such as the possibility to obtain data only in supine position, the invasiveness of the measurement and the difficulty to perform dynamic acquisitions. Because of that they combined an optoelectronic system of movement analysis and free-hand ultrasound scans to acquire the data and process the modelling.

The procedure was as follows. From six healthy volunteers, free-hand ultrasound (US) scanning of their abdomen was performed at two different lung volumes (functional residual capacity (FRC) and total lung capacity (TLC)) and two different postures (supine and seated). Before that the subjects were instrumented with sixteen water filled markers for anatomical location orientation. The 3D tracking of the probe and of the markers was obtained by the optoelectronic system of motion analysis. All the scans were performed during a breath-holding period of about 30 seconds. A MR scan was also performed in one subject for later validation of the method.

The second part of this study consisted of processing the US images and the three-dimensional position of the probes and to obtain the model of diaphragm. After the US scanning, the resultant US images were processed to determine the bi-dimensional coordinates of the diaphragm. However the authors did not explained how the coordinates were obtained. The 3-D reconstruc-

tion was also not sufficiently explained. They considered a semi-automatic algorithm to extract the silhouette of the diaphragm from the bi-dimensional coordinates and the three-dimensional position of the probes but they did not indicate which algorithm was used. The three-dimensional coordinates of the diaphragm were also filtered and interpolated before they proceeded to the reconstructed surface.

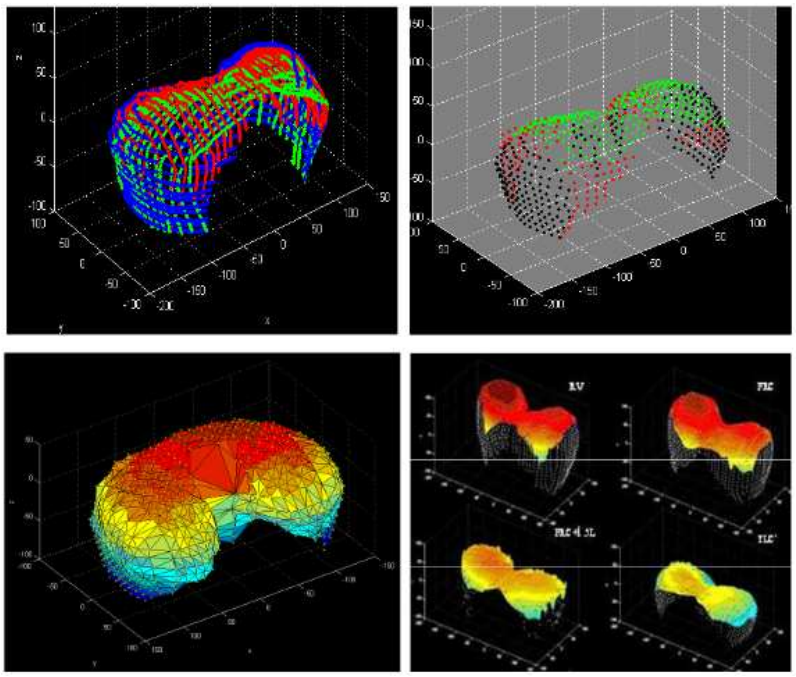

Figure 3.3: 3D plots of the silhouettes from different views (top left) and cloud of points extracted from the intersection of the different silhouettes (top right). 3D reconstruction of the diaphragm surface from posterior view (bottom left) and reconstructed the surface of the diaphragmatic dome and the cloud of points of the apposition zone at different lung volumes (bottom right) [5].

Quaranta *et al* concluded that the method based on US to obtain the 3D model of the diaphragm is reliable and accurate. Nevertheless a significant portion of the surface, mainly in the appositional zone (see Figure 3.3, bottom right), was lost because of the restricted field of view of the US probe. They observed that the diaphragm position is influenced by both lung volume and posture; at high volumes (i) the position is lower and (ii) in seated position, the diaphragmatic domes are more cranially located. The method was also verified by both MR reconstruction and literature. In fact the position and the shape of both MR and US reconstruction of the surface of the diaphragm matched each other.

Although all of the previous studies had the same starting point, which is the generation of three-dimensional objects from two-dimensional images, the main objectives of each study were quite different. In fact this is the most important advantage of modelling the diaphragm from three-dimensional reconstruction: it can be used in several studies with different subjects and objectives.

Models of the diaphragm obtained with different methods of reconstruction are widely used in research. The most used source images for modelling are magnetic resonance images and photographic images taken from cadavers. The reconstruction can be semi-automatic or totally automatic. The most used reconstruction technique is semi-automatic. The totally automatic procedure is rarely used because the segmentation of the diaphragm is a very difficult process. Indeed the diaphragm is a very thin structure difficult to detect in medical images. In almost every previous studies the authors used the contrast between organs, specifically between lungs and abdominal content, to segment the diaphragm.

## 3.2 Mechanical analysis

Worldwide both engineers and physicians together try to obtain realistic simulations of biological events in the human body. The advantages are enormous: they will allow, for example, the evaluation of the consequences that diseases or other health problems have in the human body. Mechanical analysis is one of these processes which helps to provide the tools for realistic simulations. Biomechanics of the movement tries to simulate some pathological motions in walking, running and other human movements. However in the present work the target of the numerical simulations is the respiration cycle and its consequence in the diaphragm.

The mechanical analysis provides the response of materials or assemblies and is considered the first step in putting a critical design into practice. In biomedical engineering it provides stresses, strains and displacements of organs due to different loadings and situations. Indeed the evaluation of the mechanical response is very important for the knowledge of the physiology of the body and can help physicians in practical medicine such as in surgeries [23].

The biomechanical analysis performed in the present work uses the finite element method (FEM). Because the diaphragm is a complex three-dimensional organ, both geometrical and mechanically, FEM is a good tool for the necessary numerical simulations. ABAQUS$^{TM}$ is the software package used to performed the FEM study in the present work.

Martins *et al* [24] and D'Aulignac *et al* [23][25] used the FEM to study the pelvic floor muscles. In fact they propose, improve and test a 3-D muscle model based on the one-dimensional Hill-type muscle model. This new model is an improvement of the muscle model proposed earlier by Humphrey and Yin [26] which was originally conceived for cardiac muscles. The muscle model used in these studies is also the one used in the present thesis and it will be described in the next chapter.

In these studies the model has been improved and tested under different conditions. In their studies, D'Aulignac *et al* [23][25] presented the muscle model and performed simulations of the levator ani muscle under pressure and with active contraction. The geometrical model of the levator ani muscle used was obtained from cadaver measurements which were available in the

literature. The authors concluded that the levator ani muscle model alone is not enough to correctly characterize the pelvic floor. They suggest to add additional substructures to obtain more reliable simulations. They also found that the muscle model detected high stress values at the sling attachment points of the levator ani which is where the most post-partum lesions occur.

In more recent studies Martins *et al* [7][27] and Pato & Areias [28] improved and generalized the constitutive model. Such model was mainly applied to the study of the pelvic floor. The improvements showed to be relevant to model faster contractions, which may occur in intervals of time of the same order of the muscle activation and deactivation times.

### 3.2.1 Motion functional analysis - Physically based analysis

Although the physically-based analysis main purpose is the model and the real-time animation, it also describes the motion of an object very well.

As referred in the previous section (subsection 3.1.4) Promayon *et al* [2] presented a study of a 3D functional model of the diaphragm in order to illustrate mechanical aspects of the contraction and reproduce the piston motion of the diaphragm. They have used a physically based model implemented in the software *Phymul* to create the geometry of the objects and simulate their behaviour in a certain period of time. Indeed all the relevant data such as forces, weight, regions of the diaphragm and the constitutive functions are defined in this routine.

Relatively to the model definition, *Phymul* permits the creation of distinct regions which is important to separate the different organs of the human trunk and specify the corresponding types of tissue. Additionally different forces and constraints can be separately applied to those independent regions. The regions are composed of elements which contain all the relevant information. *Phymul* has also a functional division and a characterization of the model. All the elements and regions are separated and well represented in a functional hierarchical structure: a general region is on top, in the middle level are the solid and the elastic regions and included in the latter is the muscular region. Therefore this hierarchical structure allows the physically-based model to choose efficiently the appropriate properties of each element in the region to which it belongs. Inside each region each element is linked to its neighbours by a mass-spring system. Additionally the linkage of elements of different regions is also characterized by this system but take into account the hierarchy structure. Each region will be affected by the neighbouring regions that will influence the resultant displacement. With respect to the laws of dynamics, both forces and masses are applied to the nodes of each element. The masses are equally distributed by the elements and in each element by the nodes. In this study [2] Promayon *et al* estimated a diaphragm mass between 450 and 500$g$ considering a 85$kg$ weight male.

With respect to the characterization of the diaphragm, the model was divided in two main regions: a central tendon and a muscular region connected to the bone. The central tendon region was defined by the top elements of the model and it was characterized as more rigid than

the muscle to simplify the simulation. On the other hand the muscular region was characterized by a network of muscle fibres that defined as a function of contraction. The muscle fibres were directed from the insertions on the bones to the border of the central tendon. The contraction function was based on the respiratory cycle and the electric activity observed in the phrenic nerve and was represented by a contraction unit as a function of time.

The simulations used an iterative algorithm. Basically at each step of the iteration the algorithm calculates the new state as follows. For each element of each region the process determines the sum of the forces applied to the model. Secondly a system of the equations governing the movement is used to calculate an intermediate state which does not take into account the constraints. Then from this state the displacements that verify the constraints are determined. Finally the algorithm applies these displacements to the nodes of the corresponding elements and adjusts the real velocities.

It is important to note that Promayon *et al* had also to adjust the abdominal and thoracic regions by maintaining the volume under the diaphragm constant. Because of the interactions between lungs-thorax and diaphragm and between abdomen and diaphragm are not represented it was necessary to avoid the diaphragm expansion along the transverse axis and to maintain the variation of the pulmonary volume.

The different results (i.e. volume variation, $\Delta$L, $\Delta$R, $\Delta$H) obtained from the analysis of all models were generally in agreement among each other. Furthermore it was possible to determine a relationship between the function of contraction and the volume variation, which can be a good tool to identify certain pathologies.

Santhanam *et al* [29] also used a physically-based deformation model to deform a 3D lung model with time. Although the deformation method used was different from Promayon's, the simulation was able to successfully deform the high-resolution lung model. They concluded also that the method can deform the model in a real-time environment because the algorithm has a fast convergence.

## 3.3 Pathological Dysfunctions of the Diaphragm

### 3.3.1 Amyotrophic Lateral Sclerosis

Amyotrophic Lateral Sclerosis is a neurodegenerative disorder characterized by a progressive weakness of all the muscle groups in the body. This disease is progressive and in most cases it leads to death. In the majority of the cases the respiratory failure is the most common cause of death. The respiratory muscles, inspiratory, expiratory and upper airway muscles are essential for normal ventilation and in ALS they can be impaired. However several evidences point the diaphragm as an important determinant of the ALS-related respiratory insufficiency [30]. The phrenic nerve has several morphometric abnormalities and its motoneurons are located in regions

extremely affected by the disease.

The diaphragmatic dysfunction was studied by Similowski *et al* [30]. They briefly described the effect of ALS in the diaphragmatic function. They also studied these effects in patients with and without dyspnoea. The diaphragm function was measured with nonvolitional and noninvasive tests in response to cervical and cortical magnetic stimulation, such as examination of the paradoxical respiration and the respiratory pulse, ribcage and abdominal displacement and other pulmonary tests. The study was performed in 48 patients separated in two groups, one with and the other without dyspnoea.

From the cervical magnetic stimulation they obtained a decrease in the abdominal and ribcage displacement only in 36 per cent of patients in the group with dyspnoea. Relatively to the dyspnoea, only two variables, the paradoxical respiration and the cortex-to-diaphragm conduction times, in all the tests performed were associated with dyspnoea. Similowski *et al* concluded that diaphragm abnormalities were more pronounced in patients reporting dyspnoea. They also concluded that the combination of test indexes showed diaphragm weakness as a diaphragm dysfunction. The paradoxical respiration results indicated extreme diaphragm weakness but it was not clear if it was due to intrinsic diaphragm weakness or to the impaired generation or transmission of the central command.

The effect of ALS in the pulmonary function is a strong cause of concern since the majority of ALS patients die of respiratory effects. Schiffman & Belsh [31] performed a study to determine the degree of respiratory impairment of ALS patients in the time of diagnosis and the subsequent rate of evolution of the respiratory muscle weakness. They chose 36 patients with ALS that had available a pulmonary function evaluation at the time of the diagnosis. The evaluation tests executed after the diagnosis were the vital capacity, the maximum negative inspiratory pressure and the maximum positive expiratory pressure.

At the time of diagnosis 31 patients had respiratory muscle weakness evidence because at least one of the tests revealed reduction in the respective pulmonary function. However only 7 of all the patients had experienced any respiratory symptoms and the 5 patients without respiratory muscle weakness showed no symptoms. Schiffman & Belsh explained this discrepancy due to a normally large pulmonary function reserve. As expected the results of all of the three performed tests, the vital capacity, the maximum negative inspiratory pressure and the maximum positive expiratory pressure had decreased in the subsequent stages of the trial. Twenty four of the 36 patients were followed up serially and therefore the rate of decline in respiratory muscle strength could be obtained. The results showed that the decline was greater in the early stages of ALS than in the later stages.

Schiffman & Belsh concluded that the pulmonary function evaluation should be a common test in clinical practice performed in patients with ALS at the time of the diagnosis. The lack of pulmonary symptomatology at the time of diagnosis corroborates this premise. Additionally the

rate of pulmonary function decline can be measured at the same time because of its quasi-linear pattern.

On the other hand Stewart *et al* [32] also performed an evaluation of the respiratory muscles based on electromyography (EMG) in patients with ALS. They also compared these results with the normal respiratory function tests, performed at the time of the diagnosis. They restricted the analysis to the diaphragm of 52 patients (one group of abnormal diaphragmatic EMG patients and another group of normal diaphragmatic EMG patients) because they considered the diaphragmatic dysfunction as the main responsible dysfunction for respiratory failure in ALS.

The results of the pulmonary tests unanimously confirmed that the patients with abnormal diaphragmatic EMG had worse performance than the patients with normal diaphragmatic EMG. The number of mortality cases was also given and 70 per cent of the 52 patients were confirmed to be deceased as a consequence of their ALS. Stewart *et al* concluded that the EMG measurement in patients with ALS at the time of the diagnosis is a good and safe test to monitor the respiratory conditions.

The respiratory abnormalities are experienced by ALS patients at one time during the disease. Indeed this issue is the main subject of many studies about ALS pathology. When the pulmonary disorder reaches a level such that the patient can no longer breath by himself, there are some techniques that help to prolong the patients life. Indeed these techniques are the main palliative treatment chosen in the cases of respiratory insufficiency [10]. Although there are some studies that indicate that the assisted ventilation induces diaphragmatic dysfunction [33], non-invasive ventilation increase survival and quality of life of ALS patients [32].

The diaphragm is the only inspiratory muscle active during the rapid eye movement (REM) sleep and therefore the risk of a respiratory disorder in sleep is high in patients with ALS. Arnulf *et al* [34] performed a study to verify the hypothesis that the diaphragm dysfunction in ALS is associated with the changes in sleep. They studied 21 patients with ALS and separated them in two groups according to the presence or absence of diaphragmatic dysfunction.

Arnulf *et al* were able to establish that the duration of the REM sleep in the majority of the patients with diaphragmatic dysfunction has dramatically been reduced, comparatively to the patients without the dysfunction. They also found that the frequency of awakenings after sleep was significantly higher in patients with dysfunction and the survival time of these patients was shorter than that of the patients without diaphragmatic dysfunction. Curiously in the former group the patients with quasi-absent REM sleep had a even shorter period of survival.

### 3.3.2 Complete Phrenic Nerve Lesion

The nervous system and the diaphragm are connected by the left and right phrenic nerves which innervate the corresponding hemidiaphragm. When the phrenic nerve is severely damaged the diaphragm paralyses. The causes can be an acute phrenic nerve injury [35], such as an

inflammation of the phrenic nerve or an accidental resection in a surgery. However when only one phrenic nerve is paralysed, the lesion is unilateral. Several studies have been performed to obtain the respiratory consequences encountered in the unilateral paralysis of the diaphragm.

Marie *et al* studied these issues in animals [36][37]. In a recent study developed in dogs [37], Marie *et al* evaluated the effect of the upper phrenic nerve root resections, unilateral and bilaterally, on the diaphragm. The resections were made in the C5 right phrenic nerve root to the unilateral group and in the C5 phrenic root to the bilateral group. The resultant evaluation of the diaphragm after the period of trial was significantly more severe in animals with unilateral resection comparatively to animals with bilateral resection. Particularly the EMG tests showed severe alterations predominantly in the sternal and the costal anterior regions of the right hemidiaphragm and in the costal medial and costal posterior of the left hemidiaphragm in the group of animals with bilateral resection. The atrophy of the right hemidiaphragm of the animals in the unilateral group was minimal while in the other group, both left and right hemidiaphragm became atrophic.

Marie *et al* concluded that the animals with a partial denervated diaphragm had similar pulmonary performance relative to animals with normal enervated diaphragm. Indeed in a hemidiaphragmatic paralysis the inactive hemidiaphragm moves caudally and then cranially. This movement is determined by the force generated by the healthy hemidiaphragm and by the pleural pressure. In the intact hemidiaphragm the distribution of strengths around its surface changes because of the unequal distribution of residual innervation. The comparison of the results of both bilateral and unilateral upper phrenic nerve root resection showed that the bilateral resection induces more severe diaphragmatic dysfunction than the unilateral resection. The authors could not explain this result but suggested that cross-innervation or reinnervation is responsible for this phenomenon.

Similar conclusion was obtained by Marie *et al* in a selective resection study performed in rabbits [36]. The diaphragmatic function was preserved after the resection of the highest root of the phrenic nerve.

Shindoh *et al* [35] also studied the effect of the unilateral resection of the phrenic nerve in the contraction of the diaphragm. They concluded that the nerve supply in the muscle of the diaphragm is a determinant factor of the muscle contractile properties and also of the muscle fibre composition. Comparatively to intact diaphragm, the unilateral phrenic nerve denervation showed a significantly decrease in the contraction force and time of the denervated hemidiaphragm and also a reduction of the cross sectional area of the fast-twitch fibres.

In humans, Laroche *et al* [38] also studied the diaphragm strength in patients with hemidiaphragm paralysis. Eleven patients experiencing recent unilateral diaphragm paralysis were monitored. The results showed a reduction of the exercise tolerance in 9 patients. The transdiaphragmatic pressure and the time of phrenic nerve conduction in the affected side of the diaphragm decreased during pulmonary tests which is consistent with phrenic nerve dysfunction. Although

the pathological condition of unilateral resection causes increase in breathlessness and decrease in exercise tolerance, the patients could breath by themselves and the authors did not refer any necessary auxiliary ventilation.

# 4

# Muscle Model

## Contents

In this Chapter the mechanical behaviour of the muscle is addressed. The mechanical model adopted in the present work is presented as well as the corresponding constitutive equations.

## 4.1 Skeletal Muscle - physiology

As mentioned before, the diaphragm is formed by two main types of tissue: a tendinous part and a skeletal muscular part. The tendinous part is modelled as a linear elastic isotropic material.

On the other hand the muscle part of the diaphragm is generally considered a transversely isotropic material [7]. Skeletal muscles have a complex mechanical behaviour because they are essentially incompressible and have a single muscle fibre direction. Also activation processes may take place along the muscular fibres due to neural stimulation.

The skeletal muscle is composed of many fibres which extend throughout the muscle length [6]. The fibres are connected to tendon which is linked to bones. Each fibre of the muscle is formed by subunits. The smallest subunit, the sarcomere, is responsible for the muscle contraction and is composed of actin and myosin. The actin and myosin proteins are filaments constituted by G actin and myosin molecules, respectively. Figure 4.1 shows an illustration of bounded sarcomeres in relaxed and contracted states: when a contraction occurs the myosin filaments slide along the actin filaments and the muscle length is shortened. The actin filaments are attached at one end but are free along their length to slide with respect to the myosin filaments and to make and break chemical connections, cross-bridges, at different locations with the heads of the molecules of myosin: this is the process that is responsible for active contraction and force generation in the muscles.

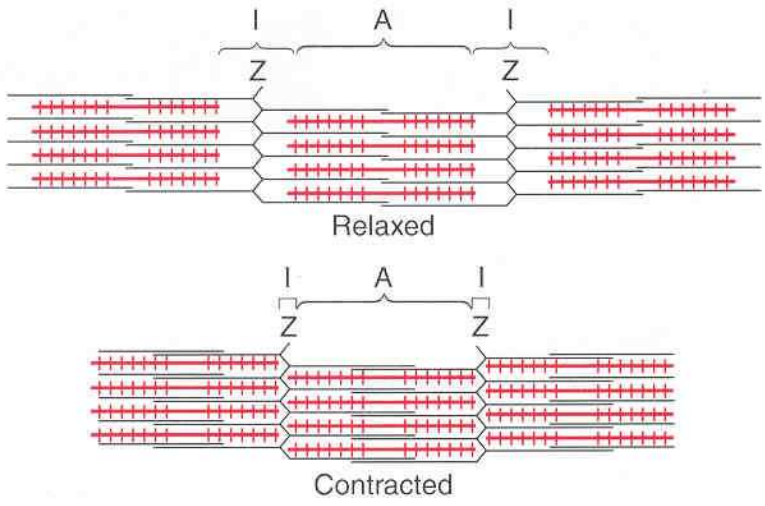


Figure 4.1: Relaxed (top) and contracted (bottom) state of a myofibrile with three sarcomeres. The zones labelled with I (from isotropic) are white bands containing actin filaments only. The A labels (from anisotropic) represent the bands with myosin filaments and the edges of actin filaments. The Z disk is where the actin filaments from adjacent sarcomeres get together [6].

The muscular contraction is a process that starts in a motor neuron and ends in the contraction itself. Guyton & Hall [6] described the muscular contraction as having seven essential steps: after an action potential from a motor neuron arrives at the muscular fibres (i), a small number of acetilcoline (a neurotransmitter) molecules are secreted (ii). The function of this neurotransmitter is to open multiple channels in the muscular fibre membrane. When these channels are opened, a large amount of sodium ions is released inside the muscular fibre membrane (iii). This phenomenon creates an action potential that propagates along the muscular fibre membrane in the same way as this action potential is propagated along the neural membranes (iv). At each place of the membrane the electricity generated by the depolarized action potential is also propagated inside the muscular fibre. As a consequence the sarcoplasmatic reticulum located inside the fibres releases a large amount of calcium ions (v). These ions are responsible for the slide of myosin relative to the actin: it generates attractive forces between the myosin and actin filaments leading to the contractile process (vi). Finally, a fraction of seconds later, the calcium ions return to the sarcoplasmatic reticulum ceasing the contraction process (vii).

This theory of muscular contraction is essential in simulating the skeletal muscle behaviour. In fact the one-dimensional nature of the fibres (actin and myosin only slide along one direction) has been the focus of much of the research on the skeletal muscle's contraction. And in this field the most well known of the proposed models is the Hill muscle model.

## 4.2 Hill's muscle model

Although there are more than one Hill's muscle model [39] the most common version is a model composed of three elements: a (active) contractile element (CE) in series with a (passive) elastic element (SE), both of them in parallel with another (passive) elastic element (PE) (see Figure 4.2). The contractile element is the active component of the model, it represents the actin and myosin filaments sliding relative to each other and the active force generated is a result of the number of active cross-bridges between the filaments. This element is responsible for the free change in length of the muscle (when non-activated) and for the force generation in the muscle (when activated) [7]. On the other hand the elastic element SE represents the connective tissue in series with the sarcomeres including the tendon while the parallel elastic element represents the parallel connective tissue surrounding the contractile element [40].

In Hill's model the longitudinal muscle stress is the sum of the stresses in the parallel and series elements [7]

$$T = T_{PE} + T_{SE} \tag{4.1}$$

while the stress in the contractile element is equal to the stress in the series element

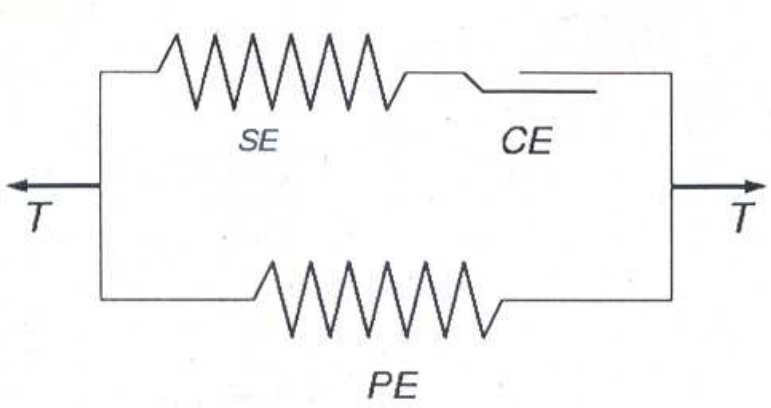


Figure 4.2: Hill's three element muscle model. T is the muscle stress while SE, CE and PE are series, contractile and parallel elements respectively [7].

$$T_{CE} = T_{SE}. \tag{4.2}$$

Also

$$\Delta L_{SE} = \Delta L_{PE} - \Delta L_{CE} \tag{4.3}$$

where $\Delta L_{CE}$, $\Delta L_{PE}$ and $\Delta L_{SE}$ are the corresponding length changes from the rest length.

In Martins *et al* [7] the stress in the contractile element is the product of three main functions. One is a function of the contractile stretch which has a typical bell or inverted parabola shape, with maximum value at the muscle rest length. The second is a function of the strain rate of the contractile element which, for contracting rates, corresponds to Hill's hyperbolic law. The last one is a function of an activation variable $\alpha$ varying between 0 and 1. This variable represents the dynamics of concentration of the calcium ions along the muscle fibres. The other two stresses, in the series and parallel elements, are highly non-linear functions of their elongations and essentially vanish in compression. Thus the governing equation for the contraction process can be represented as a first order differential equation

$$\dot{T} = \mathcal{T}(T, \lambda, \dot{\lambda}, \alpha) \tag{4.4}$$

where $T$ is the muscle stress, $\lambda$ and $\dot{\lambda}$ are the muscle stretch and stretch rate and $\alpha$ can be represented as another first order ordinary differential equation

$$\dot{\alpha} = \mathcal{A}(\alpha, u) \tag{4.5}$$

where $u$ is a scalar control variable varying between 0 and 1 representing the excitation from the neural signal.

## 4.3 From 1D to 3D models

In the first simulations performed only 1D models were considered. Linear stretches and contractions were tested under various Hill-based models. However in recent years two- and three-dimensional models started to be proposed and studied. Although the first 3D models were not detailed and accurate enough for medical needs because the main motivations involved only animations and entertainment purposes, quickly the models began to improve.

The major difficulty in passing from 1D muscle models to the 2D and 3D simulation cases was essentially the lack of experimental information on the transversal behaviour of the skeletal muscles. Relatively to the longitudinal (tension) behaviour of muscle fibres the 1D muscle models are easily used in 2D and 3D models because the fibre directions are well characterized in space.

In the absence of information on the transversal behaviour of skeletal muscles several authors considered in their studies two other contributions [7], besides the longitudinal, which are related to the incompressibility or quasi-incompressibility of the muscle and to an assumed embedding matrix.

## 4.4 Constitutive Equations

In the present work Hill's muscle model is adopted. Furthermore the constitutive equation which characterizes the muscle is adopted from previous studies developed by Martins *et al* [7], D'Aulignac *et al* [23] [25] and Pato & Areias [28]. This model is a modified form of the incompressible transversely isotropic hyperelastic model proposed earlier by Humphrey and Yin [26] for passive cardiac muscles in which the behaviour of the 1D Hill-type model is assigned to the muscle fibres.

The constitutive equation for the Cauchy stress tensor $\boldsymbol{\sigma}$ is of the form

$$\boldsymbol{\sigma} = \boldsymbol{\sigma}_{incomp} + \boldsymbol{\sigma}_{matrix} + \boldsymbol{\sigma}_{fibre}. \tag{4.6}$$

The first contribution is related to the incompressibility of the material and is given, in the case of perfect incompressibility, by

$$\boldsymbol{\sigma}_{incomp} = -p\mathbf{I} \tag{4.7}$$

where $p$ is the hydrostatic pressure and $\mathbf{I}$ is the identity tensor.

The matrix contribution $\boldsymbol{\sigma}_{matrix}$ is typically isotropic hyperelastic, similar to those adopted in other soft tissues. This contribution has the same exponential form adopted by Humphrey & Yin [26], but with material parameters obtained in some compression experiments with skeletal muscle available in the literature [42]. It is of the form

$$\boldsymbol{\sigma}_{matrix} = 2bc \exp\left[b\left(I_1^C - 3\right)\right] dev\left[\mathbf{B}\right] \tag{4.8}$$

where $b$ and $c$ are constants, $\mathbf{B}$ is the left Cauchy-Green strain tensor $\mathbf{B} = \mathbf{F}\mathbf{F}^T$, $\mathbf{F}$ is the deformation gradient,

$$I_1^C = tr\left(\mathbf{C}\right)$$

is the first invariant of the right Cauchy-Green strain tensor $\mathbf{C} = \mathbf{F}^T\mathbf{F}$ and

$$dev\left[.\right] = (.) - \frac{1}{3} tr\left(.\right)\mathbf{I}$$

is the deviatoric operator in the current configuration.

The last contribution to the Cauchy stress is the muscle fibre contribution which is given by

$$\boldsymbol{\sigma}_{fibre} = dev\left[\lambda_f T \mathbf{n} \otimes \mathbf{n}\right] \tag{4.9}$$

where $\lambda_f$ represents the stretch ratio in the the muscle fibres which have the direction of the unit vector $\mathbf{N}$ in the undeformed configuration.

$$\lambda_f = \sqrt{\mathbf{N}^T \mathbf{C} \mathbf{N}}.$$

The scalar $T$ represents the nominal stress in the fibre (the force in the fibre per unit area of the cross section of its reference rest configuration) and the unit vector $\mathbf{n}$ indicates the direction of the muscle fibres in the deformed configuration

$$\mathbf{n} = \frac{\mathbf{F}\mathbf{N}}{\lambda_f}.$$

Because of the large deformations involved, a decomposition of the stretch ratio of the muscle fibres $\lambda_f$ into a multiplicative split of the contractile stretch $\lambda^{CE}$ followed by an elastic stretch (from the series element) $\lambda^{SE}$ is considered [7]

$$\lambda_f = \lambda^{CE}\lambda^{SE}. \tag{4.10}$$

This mathematical split is also a physiological split. Considering an initial fibre length $L_0$, a deformed fibre length $L^C$ due to the relative sliding in the actin-myosin contractile device and a final length $L$ due to the elastic deformation of those myofibres superposed to their relative sliding then

$$\lambda_f = \frac{L}{L_0}, \quad \lambda^{CE} = \frac{L^C}{L_0}, \quad \lambda^{SE} = \frac{L}{L^C} \tag{4.11}$$

This approach has also the advantage that it does not require the knowledge of microscopic information on the partition of the initial fibre length between the series elastic and the contractile elements and, as referred before, approximates the constitutive theory of muscle behaviour to the framework of large deformation continuum mechanics with internal variables ($\lambda^{CE}$ is one of the internal variables).

The present approach considers that the strain energy of the muscle is stored isotropically in the material as well as in the direction of the muscle fibres

$$U = U\left(\mathbf{C}, \lambda^{CE}\right) = \underbrace{U_{matrix}\left(I_1^C\right)}_{U_I} + \underbrace{U^{PE}\left(\lambda_f\right) + U^{SE}\left(\lambda^{SE}, \lambda^{CE}\right)}_{U_f} \tag{4.12}$$

where $U_I$ and $U_f$ correspond to the stress contributions (4.8) and (4.9), respectively. Therefore the Cauchy stress tensor can also be given as

$$\boldsymbol{\sigma} = -p\mathbf{I} + 2dev\left[\mathbf{F}\frac{\partial U}{\partial \mathbf{C}}\mathbf{F}^T\right]. \tag{4.13}$$

The stress $T_{PE}$ in the parallel elastic element is given by

$$T_{PE}(\lambda_f) = T_0 f^{PE}(\lambda_f) \tag{4.14}$$

where $T_0 = F_0/A_0$ represents the maximum tensile stress produced by the muscle at resting length ($F_0$ is the maximum force and $A_0$ is the physiological cross-sectional area) and $f^{PE}$ is given by

$$f^{PE}(\lambda_f) = \begin{cases} 2aA\exp\left[a\left(\lambda_f - 1\right)^2\right]\left(\lambda_f - 1\right), & \lambda_f > 1 \\ 0, & otherwise \end{cases} \tag{4.15}$$

where $a$, $A$ are constants.

The stress $T_{SE}$ in the series element is defined as

$$T_{SE}(\lambda^{SE}, \lambda^{CE}) = T_0 f^{SE}(\lambda^{SE}, \lambda^{CE}) \tag{4.16}$$

where $f^{SE}$ is given by

$$f^{SE}(\lambda^{SE}, \lambda^{CE}) = 0.1\left\{\exp\left[100\lambda^{CE}\left(\lambda^{SE} - 1\right)\right] - 1\right\}, \lambda^{SE} \geq 1. \tag{4.17}$$

Finally the stress $T_{CE}$ in the contractile element is given by

$$T_{CE}(\lambda^{CE}, \dot{\lambda}^{CE}, \alpha) = T_0 f_L^{CE}(\lambda^{CE}) f_V^{CE}(\dot{\lambda}^{CE})\alpha \tag{4.18}$$

where $f_L^{CE}$ and $f_V^{CE}$ represent the dependence of the contractile stress on the contractile stretch $\lambda^{CE}$ and on its time rate of change $\dot{\lambda}^{CE}$, respectively. These functions are of the form [28]

$$f_L^{CE}(\lambda^{CE}) = 8 \begin{cases} \left(\lambda^{CE}\right)^2 - \lambda^{CE} + 0.25, & 0.5 \leq \lambda^{CE} < 0.75 \\ -\left(\lambda^{CE}\right)^2 + 2\lambda^{CE} - 0.875, & 0.75 \leq \lambda^{CE} < 1.25 \\ \left(\lambda^{CE}\right)^2 - 3\lambda^{CE} + 2.25, & 1.25 \leq \lambda^{CE} < 1.5 \\ 0, & otherwise \end{cases} \tag{4.19}$$

$$f_V^{CE}(\dot{\lambda}^{CE}) = \begin{cases} \left(\dot{\lambda}^{CE} + 10\right)\epsilon, & \dot{\lambda}^{CE} < -10 \\ -\frac{\arctan\left(-0.5\dot{\lambda}^{CE}\right)}{\arctan(5)} + 1, & -10 \leq \dot{\lambda}^{CE} \leq 2 \\ \left(\dot{\lambda}^{CE} - 2\right)\epsilon + \frac{\pi}{4\arctan(5)} + 1, & \dot{\lambda}^{CE} > 2 \end{cases} . \tag{4.20}$$

It is important to note that in the present study the horizontal branches (when $\dot{\lambda}^{CE} < 10$ and $\dot{\lambda}^{CE} > 2$) will be replaced by branches with a small slope for computational purposes. Consequently the function $f_V^{CE}$ will be strictly monotone and invertible in $\mathbb{R}$. Thus the time rate of change of the internal variable $\lambda^{CE}$ is governed by the ordinary differential equation

$$\dot{\lambda}^{CE}\left(\lambda_f, \lambda^{CE}, \alpha, \dot{\lambda}_f, u\right) = f_V^{CE^{-1}}\left(\lambda_f, \lambda^{CE}, \alpha, \dot{\lambda}_f, u\right). \tag{4.21}$$

The activation process results from neural stimulation and characterizes the contractile element. As referred in equation (4.5) the activation variable $\alpha$ is governed by the first-order ordinary differential equation. In this work the ODE proposed by Pandy *et al* [41] is adopted:

$$\dot{\alpha}(t) = \frac{1}{\tau_{rise}}\left\{1 - \alpha(t)u(t) + \frac{1}{\tau_{fall}}\left[\alpha_{min} - \alpha(t)\right]\left[1 - u(t)\right]\right\} \tag{4.22}$$

where $\tau_{rise}$ and $\tau_{fall}$ are the characteristic time constants for activation and deactivation of the muscle, respectively, $\alpha_{min}$ is the minimum value of the activation and $u(t)$ is a function with values between 0 and 1 and represents the neural excitation. The activation function $\alpha(t)$ ranges from $\alpha_{min} \geq$0 to 1.

To solve numerically the two ODEs (4.21) and (4.22) the backward-Euler scheme is used.

## 4.5 Simplification of the model

In the current study the diaphragm is modelled as a shell because its thickness is very small (between $3mm$ and $5mm$). Therefore it is possible to obtain a simplified muscle model for the active and passive behaviour of this skeletal muscle by modifying the above 3D model in order to agree with the thin shell theory.

In the plane stress case and for a shell without shear deformation, the left $\mathbf{B}$ and right $\mathbf{C}$ Cauchy-Green tensors used in (4.8) are, respectively, given by

$$\mathbf{B} = \begin{bmatrix} \underbrace{\mathbf{F}_p\mathbf{F}_p^T}_{\mathbf{B}_p} & 0 \\ 0 & F_{33}^2 \end{bmatrix}, \mathbf{C} = \begin{bmatrix} \underbrace{\mathbf{F}_p^T\mathbf{F}_p}_{\mathbf{C}_p} & 0 \\ 0 & F_{33}^2 \end{bmatrix}$$

where the direction 3 corresponds to the normal of the middle surface of the shell and

$$\mathbf{F} = \begin{bmatrix} F_{11} & F_{12} & 0 \\ F_{21} & F_{22} & 0 \\ 0 & 0 & F_{33} \end{bmatrix} = \begin{bmatrix} \mathbf{F}_p & 0 \\ 0 & F_{33} \end{bmatrix}.$$

Furthermore the perfect incompressibility condition implies that $J = \det \mathbf{F} = 1$ and then

$$F_{33} = \frac{1}{\det\left[\mathbf{F}_p\right]}.$$

Consequently the first invariant $I_1^C$ in (4.8), the stretch ratio in the reference configuration $\lambda_f$ and the corresponding direction in the deformed configuration $\mathbf{n}$ reduce, respectively, to

$$\begin{aligned} I_1^C &= tr\left(\mathbf{C}_p\right) + C_{33} \\ \lambda_f &= \sqrt{\mathbf{N}_p^T\mathbf{C}_p\mathbf{N}_p} \\ \mathbf{n}_p &= \frac{\mathbf{F}_p\mathbf{N}_p}{\lambda_f}. \end{aligned}$$

Considering the plane stress condition $\sigma_{33} = 0$ in equation (4.13), the hydrostatic pressure $p$ is given by

$$p = \frac{1}{3}\left[2U_I^{'}\left(tr\left[\mathbf{B}_p\right] - 2C_{33}\right) + \lambda_f U_f^{'}\left(\mathbf{n}_p \otimes \mathbf{n}_p\right)\right] \tag{4.23}$$

with $U_I^{'} = \frac{\partial U_I}{\partial I_1^C}$ and $U_f^{'} = \frac{\partial U_f}{\partial \lambda_f}$. Finally the Cauchy stress tensor in the plane is simply

$$\boldsymbol{\sigma}_p = 2U_I^{'}\left(\mathbf{B}_p - B_{33}\mathbf{I}_p\right) + \lambda_f U_f^{'}\left(\mathbf{n}_p \otimes \mathbf{n}_p\right). \tag{4.24}$$

# 5

# Computational Model and Simulations

## Contents

In the present chapter the computational model is presented. The first part of the chapter deals with the three-dimensional reconstruction of the diaphragm, from sectional planar images of the relevant zones of the body to the final 3D finite element model of the diaphragm. Then the evaluation of the direction of the muscle fibres is considered. These directions are an input for the muscle model. Finally the different analyses performed are referred. They consist of (i) a normal and quiet breathing test and (ii) two pathological quiet breathing tests. In the normal and quiet breathing case all motor units can be activated while in the two pathological cases there is loss of motor units.

The muscular part of the diaphragm has different mechanical properties than those of the tendinous part. The latter is assumed to be isotropic linear elastic while the former is based on the model proposed by Martins *et al* [7][28][24]. Besides several parameters available in the literature [28] it is necessary to obtain the direction of the muscle fibres. It is also necessary to provide as an input for the model the muscular excitation, $u(t)$. This neural stimulation plays an important role in the breathing cycle.

## 5.1 3D Reconstruction

### 5.1.1 Image Acquisition

In the present section the reconstruction of the diaphragm is explained.

The diaphragm is a very thin membrane situated at the toraco-abdominal part of the body. Its visualization in classical medical images such as MRI, X-ray or ultrasound images is very difficult to perform. In MRI and X-ray images the soft tissues are almost indistinct from each other and even in ultrasound images its observation is conditioned. Additionally the small thickness of the diaphragm results in its camouflage, visually blended with the surrounding organs on these images.

On the other hand the images of the Visible Human Project are real sectional images of a frozen cadaver which display the different organs in true colour. Indeed it is easier to identify anatomically the organs in these images. For these reasons only the VHP images are considered in order to obtain the segmented diaphragm.

The Visible Human Project provides two types of data: one from a 59 year-old female cadaver and another from a 38 year-old male body. Despite of all the differences between the two donors they both were considered healthy and had the minimum medical requirements for the project. Therefore the choice of the image data from the male or the female donor is not relevant. In the present study the female specimen is considered (Figure 5.1).

The data available from the Visible Human Female Project was downloaded in a native format and converted to a more common and readable tagged image file format (TIFF). This format is readable by common software programs responsible for image editing and it also presents high

Figure 5.1: Image of the reformatted coronal section of the Visible Human Female body [8].

spatial resolution images. The downloaded data corresponds to blocks of transversal sections of the thorax and abdomen. In fact it was necessary to separate the zones of these blocks that are considered of interest to the model: between the inferior part of the lungs' cavity and the superior part of the kidneys. This resulted in 943 axial images that correspond to a total vertical length of 298.65$mm$.

### 5.1.2 Segmentation

The next step in the reconstruction is the segmentation. This process is a very time consuming procedure because it requires manual work without any automatic computational interference.

Segmentation was necessarily performed by visual inspection along the transversal sections (for the lateral parts) and the sagittal sections (for the diaphragm body). Due to the vertical anatomy of the lateral zones the segmentation of the sagittal images was impracticable. Thus the selected axial images were computationally reformatted with MatLab™ to obtain sagittal images of the region under study (Figure 5.2).

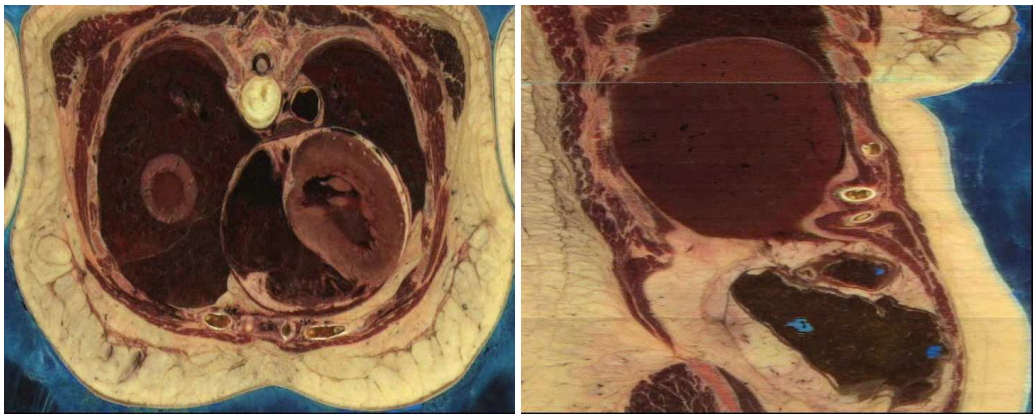

**(a)** **(b)**

Figure 5.2: The thirteenth axial (a) and the one hundred and twentieth reshaped sagittal (b) images of the region of interest. The right dome of the diaphragm is visible in both images: in the top of (b) and in the middle left side of (a).

In each image the diaphragm is identified by observation and the contours are chosen to delimit the muscle. However it is necessary to impose some conditions. First only images multiple of 25 were considered for the segmentation of the diaphragm. This led to a more rapid segmentation but also to an increase in the distance between consecutive images and between the corresponding segmentation curves. The accuracy of the model also decreases. Second it was assumed that the diaphragm is represented in all images by the outside line of its thin membrane. Although the thickness of the diaphragm is perceptible in the images, it was disregarded in comparison with its other dimensions. Thus the diaphragm can be represented as a shell or a membrane. Finally it was necessary to interpolate some points because of the lack of information relative to

the horizontal cut through the middle of the liver inherited from VHP (the “black space” shown in Figure 5.1). The interpolation is performed between the two images in the extremities of this space in the sagittal plane. All of these procedures were done with Blender, an animation-based free software which has various tools for image, animation and modelling processing.

The next step deals with the generation of splines from the obtained points. In each plane corresponding to a segmented image, the selected points are connected adjacently with common splines. This process was performed in Rhinoceros™, a 3D modelling software which is able to create, edit, analyse and animate curves, surfaces and solids. Since the two borders of the diaphragm in each planar image were difficult to identify, the segmentation curves were extended near their extremities. This extension was validated by an anatomist and a physician.

From the segmented images five sets of curves were created: one in the sagittal plane and the others in the axial plane (Figure 5.3). The sagittal curves represent almost the totality of the anterior, posterior and superior part of the diaphragm. The two lateral sets of curves (2 and 3 in Figure 5.3) denote the more vertical part of the diaphragm, called apposition zone, while the other two axial sets of segments represent the pillars of the diaphragm. The sagittal images were very useful in the determination of most of the diaphragm. In fact, in the axial plane, the diaphragm is difficult to identify.

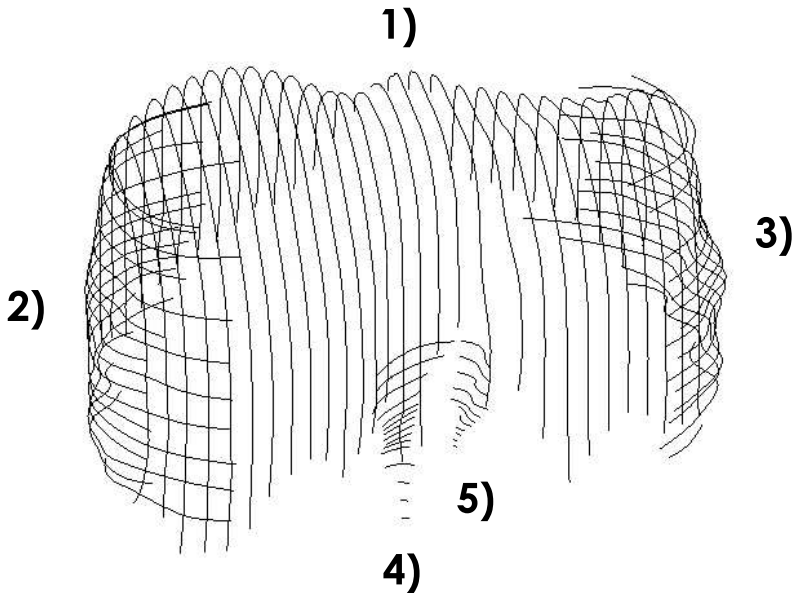


Figure 5.3: Five sets of curves identifying the diaphragm: 1) Sagittal; 2) and 3) Axial apposition zone; 4) and 5) Axial view.

The diaphragm was meshed by interpolation and connection of adjacent curves with software Rhinoceros™. The resultant model is a refined mesh with a higher spatial resolution. The software used showed a great performance in this determination and was able to produce a shell diaphragm. However some artefacts and geometric imperfections were detected. In the appo-

sition zone the muscle has some saliences and hollows due to the presence of the ribs. These cavities were inexistent in the mesh model. More importantly, the zones where the extremities of the curves from different planes intersect were badly smoothed and the mesh presented some discontinuities. The other zone surfaces were also locally smoothed. These problems were manually corrected with Blender™ without resorting to the use of automatic algorithms.

The resultant mesh was once again analysed by an anatomist and a physician. The model was validated except with respect to the cava vein aperture. This orifice was incorrectly located along the horizontal and frontal axis. A displacement of the aperture slightly to the right to a more correct location was then performed.

The 3D model of the diaphragm obtained from Blender is shown in Figure 5.4 [43]. The surface presents a smooth appearance representing the different contact locations between the diaphragm and the [thoracic and] abdominal neighbour organs. The model represents a shell with two holes, the cava vein orifice in its top middle side slightly displaced to the right and the oesophageal aperture located in the middle and posterior side of the diaphragm. The concavity formed by the intersection of both right and left pillars represents the aorta opening. The two domes are also represented by two convex surfaces, and the right dome is higher than the left dome.

Figure 5.4: 3D model of the diaphragm from Blender.

## 5.2 From the Geometric to the Finite Element Model

The next step is to import the mesh created in Rhinoceros™ and Blender to the Abaqus™ software. The latter is a general finite element package that performs computational simulations for various engineering problems. In the current work Abaqus™ is used to mechanically simulate

the respiration cycle of the different cases in under study.

The import process also requires a pre-step procedure regarding the creation of a solid object in SolidWorks™ software. This program is a more complete 3D modeling software which has a diversity of tools for design purposes. The ScanTo3D is a tool available in SolidWorks™ that basically produces a solid object from a meshed model or from a cloud of points [44]. The advantage of this tool is the possibility of generating an object divided in small surface regions which is more easy to work in the Abaqus™ software. The diaphragm mesh was imported to SolidWorks™ and the resultant object has 628 separated geometric surface elements (Figure 5.5).

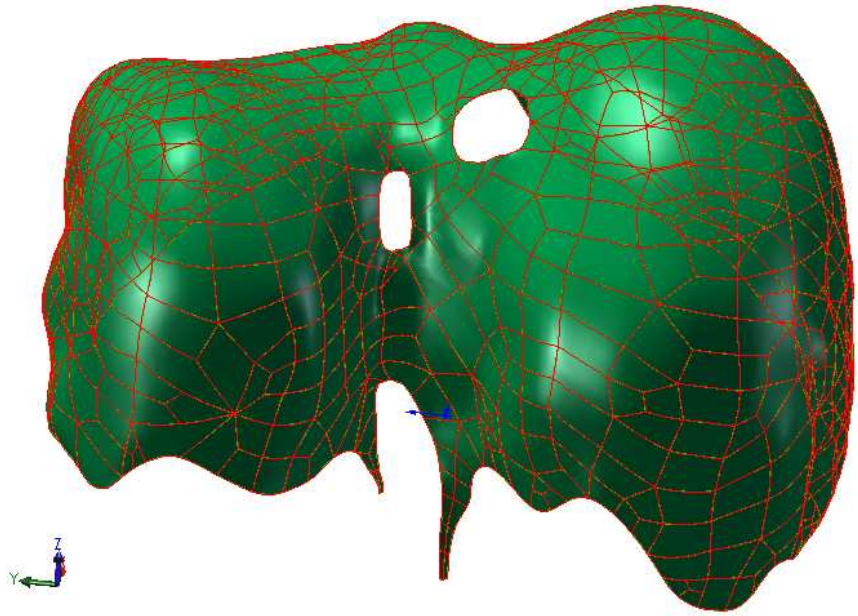


Figure 5.5: NURBS model of the diaphragm obtained in SolidWorks™.

The object created in SolidWorks™ was imported to Abaqus™ software. Additionally it was also necessary to rescale the model. The segmentation previously created was performed in the scale of the images. The maximum sagittal length of the diaphragm is the parameter used to compare and determine the scale factor. On the axial images the value of this length is 662 pixels corresponding to 218.46$mm$, since the width of the pixel is 0.33$mm$. However the value of this length in the SolidWorks™ object is approximately 11.95. Then the scale factor considered in Abaqus™ for the imported object was 18.28.

### 5.2.1 Physiological and Mechanical Considerations

The next step of the work is the definition of the mechanical and physiological aspects of the diaphragm such as boundary conditions, loads, regions of the diaphragm and material properties.

Three different main regions have to be considered for the diaphragm as mentioned in section 2.1. They are the phrenic center, the muscle and a region of tendon located in the inferior

border of the diaphragm and connecting it to the bones. This last region will further be shortly referred as *inferior tendon*. Accordingly these three main regions were generated after importing the geometric model to Abaqus™ (Figure 5.6). These three regions were identified in the model by comparing it with the 2D images of Netter [1] (see Figure 2.1). In a first approach these regions were defined according to the VHP images. However this was not an easy task to perform since the VHP images were not sufficiently accurate to identify the different tissues. Although the Netter images are only anatomic draws, they are medically validated and show the entire anatomy of the diaphragm giving a good perception of this organ.

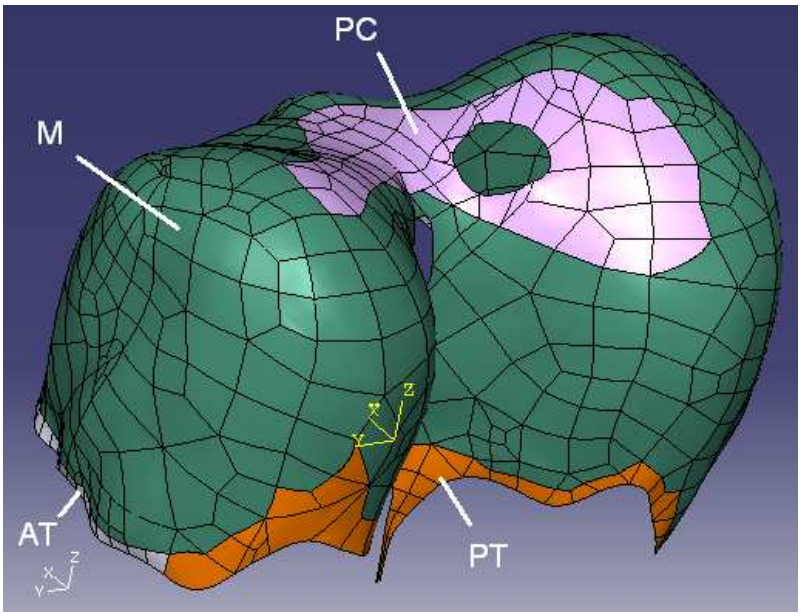


Figure 5.6: 3D solid model of the diaphragm obtained from Abaqus: PC - Phrenic Center; M - Muscle; PT - Posterior Tendon; AT - Anterior Tendon.

The central tendon was defined as the intersection of the overlapping of the phrenic center obtained from the thoracic and abdominal views. The regions obtained from both views were not coincident with each other, so a unique phrenic center was defined as the intersection of both zones. The *inferior tendon* was defined as the region in the border of the diaphragm that connects the muscle to the bones. This region is very narrow and is located along the borders. In order to better describe the inferior surface of the diaphragm, the number of geometric surface elements in this region was increased. The *inferior tendon* was also positioned at the inferior border of the diaphragm where the muscle is connected to the bone. The muscle was defined as the remaining part of the geometric model.

After the identification of each tissue in the diaphragm, their material properties are assigned to the corresponding region. The central tendon and the *inferior tendon* are defined as tendinous tissue while the muscle is characterized as muscular tissue. The tendon and the muscle are considered as homogeneous shell objects with a thickness of 3 and $5mm$ [16], respectively. The

diaphragm is too thin to carry significant bending moments or shear in the perpendicular direction relative to its main plane [45] and that is the main reason why it can be approximated by shell elements. The tendinous part of the diaphragm is considered with an elastic isotropic behaviour with values for Young's modulus and Poisson's coefficient of 33$MPa$ [16] and 0.33, respectively. The muscular tissue is modelled as mentioned in Chapter 4 with the constitutive equation given by (4.6). The parameters of the model are presented in the Table 5.1 and are chosen from Martins *et al* [7] and Pato & Areias [28], except for $\alpha_{min}$. This parameter is chosen to be 0.01 corresponding to a residual activation. Even in a relaxed state, the diaphragmatic muscle has a minimum of activity.

| Variables | Tendinous part | Muscular part |
|---|---|---|
| Young's modulus ($MPa$) * | 33 | 5.32 |
| Poisson Coefficient | 0.33 | 0.33 |
| $a$ † | - | 12.43 |
| $b$ † | - | 23.46 |
| $c$ ($MPa$) † | - | $3.79517355\times10^{-4}$ |
| $A$ † | - | $5.7270836\times10^{-4}$ |
| $T_0$ ($MPa$) † | - | 0.655868752 |
| $\tau_{rise}$ (s) † | - | $20\times10^{-3}$ |
| $\tau_{fall}$ (s) † | - | $200\times10^{-3}$ |
| $\alpha_{min}$ | - | 0.01 |
| $\epsilon$ † | - | $1.0\times10^{-4}$ |

Table 5.1: Material parameters of both muscular and tendinous tissues.

* Behr *et al* [16]
† Martins *et al* [7] and Pato & Areias [28]

A neural excitation with value $u_{max}$ is applied for a period of time of 2 seconds corresponding to the inspiration. After this period of time the neural excitation is set to zero and is maintained with this value during expiration until the end of the respiration cycle as shown in Figure 5.7.

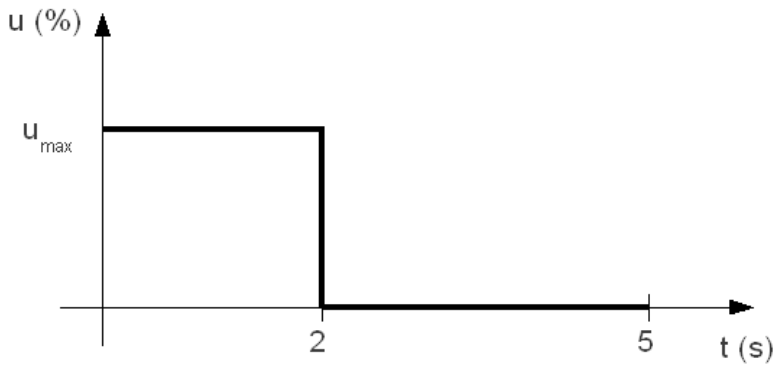


Figure 5.7: Neural excitation $u$ as a function of time.

The regions of the diaphragm were separated and became separated objects. These regions

were geometrically constrained in order for their adjacent edges to remain connected. It was necessary to create four constraints between (i) the anterior and the posterior *inferior tendon*, (ii) the muscle and both the anterior and (iii) the posterior *inferior tendon* and (iv) the central tendon and the muscle.

The boundary conditions of the diaphragm are imposed mainly in the borders of the model. In respiration the diaphragm contracts and expands according to its contraction and relaxation processes. However the contraction of the surrounding muscles and the movement of the ribs implies a relative movement of the diaphragm.

During the respiration the diaphragm follows the movement of the ribs and the sternum where it is attached. In the inspiration the thorax and the top part of the abdomen expands to the outside, anteriorly and laterally. In the posterior area the movement is not significant. In fact the vertebral column is the main responsible to prevent the expansion of the abdominal and thoracic content to the posterior outside. In the expiration the movement is quasi-symmetric, the thorax and the top of the abdomen return to the initial position of the beginning of the respiration. As a consequence of these movements, the borders of the diaphragm follow the displacement of the ribs. The borders of the diaphragm located in its anterior and lateral parts expand to the outside during the inspiration. In the expiration they return to the initial position, expanding to the inside. These movements are very complex because the variation of the displacement with time is not linear and the different zones of the borders do not displace equally. For these reasons their simulation requires an approximate knowledge of the movement of each part of the borders of the diaphragm.

In the present study, because of the complexity of the movement of the borders, the boundaries of the diaphragm are considered fixed which means that their displacements do not change with time. The borders of the diaphragm are divided in small regions for a better description of the boundary (Figure 5.8). Both the cava vein and the oesophageal apertures are constrained along the sagittal and the coronal axes. The axial displacement is kept free since the border can move along the vena cava and the oesophagus. The aortic opening is also kept constrained along the sagittal and the coronal axes being able to move freely in the axial direction. The anterior, lateral and posterior borders are all constrained in the three spatial directions preventing the movement of the diaphragm. Rotational constraints are also imposed. The apertures and the opening can rotate freely because their borders are not rotationally constrained. The posterior and the anterior lateral regions of the inferior border of the diaphragm are also free to rotate but the lateral and the anterior regions are restricted along one of the rotational axes. Both left and right lateral borders can not rotate about the sagittal axis and the anterior borders can not rotate about the coronal axis.

The pillars of the diaphragm are differently connected to the bones relatively to the rest of the borders of the diaphragm. Indeed the pillars are a tendinous tissue that connects the diaphragm

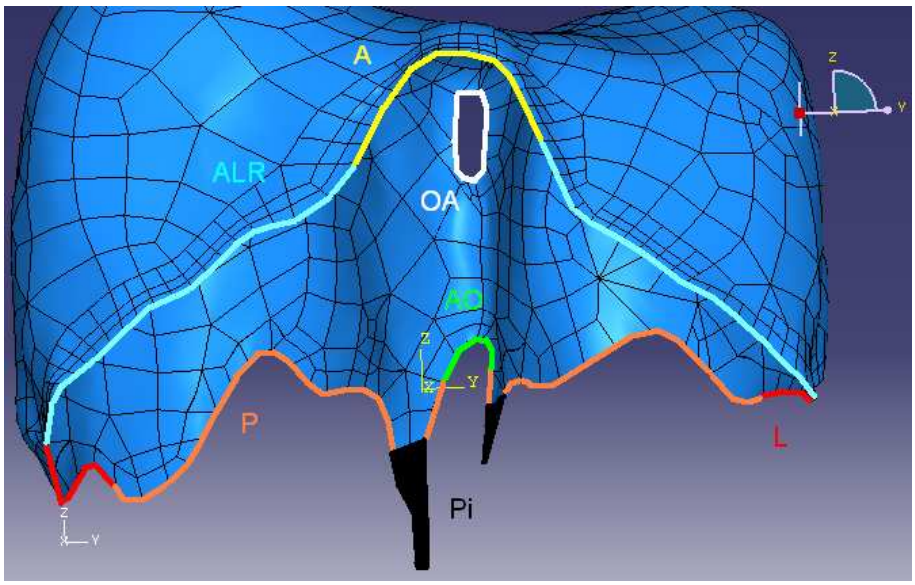


**(a)**

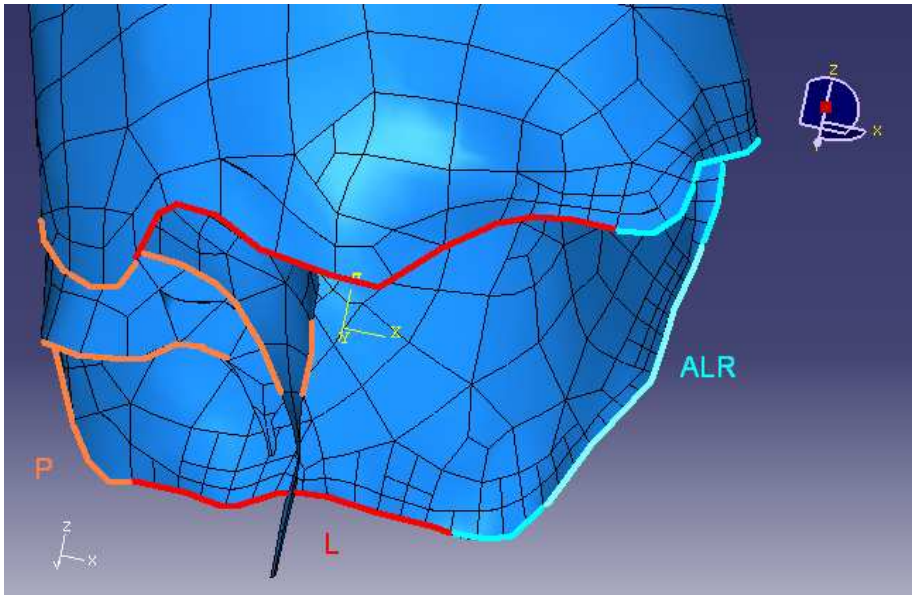


**(b)**

Figure 5.8: The division of the border of the diaphragm in boundary regions: coronal view (a); sagittal view (b). A - Anterior, ALR - Anterior Left and Right, AO - Aortic Opening, L - Lateral left and right, OA - Oesophageal Aperture, P - Posterior and Pi - Pillars.

to the vertebral column along the bodies and discs of the first three lumbar vertebrae. Therefore the boundary conditions for the pillars are such that their three spatial and three rotational degrees of freedom (d.o.f.) are totally constrained.

In the present study the load type to consider is the pressure. In medical studies the determination of the pressure profile in the surface of the diaphragm is a difficult and sometimes invasive procedure. The pressure between the inside and the outside of the diaphragmatic surfaces is called the transdiaphragmatic pressure (Pdi). Pdi is sometimes estimated by measuring the pressure in neighbouring organs (stomach, lungs,...) where it is more easy to obtain. Additionally most of the studies working with Pdi only refer values for this pressure under maximum inspiration or expiration procedures, such as the pressure in the diaphragm when lungs are filled with air in the full capacity or in the residual volume. However in the present study only a quiet breathing is considered. The Pdi in a normal and quiet breathing has a value of about $5cmH_2O$ [46] corresponding to 490.333$Pa$.

The pressure profile along the surface of the diaphragm is not uniform. However for simplification purposes only two main regions are defined and the pressure in the surface of each region is considered constant. These two regions represent the apposition and the diaphragmatic zones (Figure 5.9). In the inspiration the pressure in the apposition zone points to the outside and in the diaphragmatic zone points downwards. On the other hand during expiration the pressure in the apposition zone points to the inside and in the diaphragmatic zone points upwards.

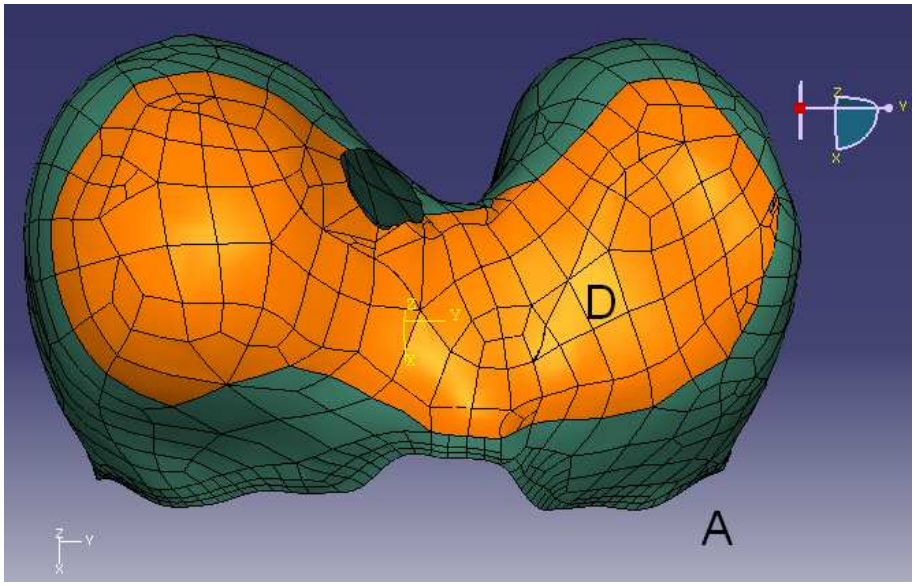


Figure 5.9: Apposition (A) and diaphragmatic (D) zones in the geometric model.

Once the solid body is obtained the meshing of the model is required. Each of the four assembled regions are meshed free and dependently. The bigger region, the muscle, was the first to be meshed. The other three were meshed according to the number of nodes of each geometric surface element in the muscle model. The finite element considered in the present study is the

S3 element which corresponds to a triangular shell element with only one integration point. The total number of elements of the model is 66,042 and the total number of nodes is 34,206 (See also Table 5.2).

| Region | Nodes | Elements |
|---|---|---|
| Central Tendon | $2,861$ | $5,384$ |
| Muscle | $28,370$ | $55,865$ |
| Anterior *Inferior Tendon* | $1,005$ | $1,442$ |
| Posterior *Inferior Tendon* | $1,970$ | $3,351$ |
| Total | $34,206$ | $66,042$ |

Table 5.2: Number of nodes and elements of each region of the meshed model.

## 5.3 Determination of the Direction of the Fibres

As previously mentioned in this chapter, the initial direction of the fibres is an input for the muscle model considered in this study. In fact it is necessary to determine the unit vector along the direction of the fibres in each element. Additionally this vector has to be in the plane of each triangular element according to a local coordinate system.

First the initial direction of the muscle fibres was obtained in a way similar to the one considered in Martins *et al* [7] and Pato & Areias [28]. In these studies the direction of the fibres is chosen to be the direction of the maximum principal Cauchy stress considering the material of the muscle to have an elastic isotropic behaviour. Figure 5.10 shows the direction of the muscle fibres obtained in this manner. Some of these directions correspond to fibres starting in the middle of the muscle as shown in the Figure 5.10. Although all of the directions show a pattern, they do not correspond to the physiological directions of the fibres.

This procedure was discarded and a new approach was considered. The direction of the fibres was determined according to a radial pattern. In fact the majority of the fibres of the diaphragm are radial, starting in the tendon of the phrenic centre and ending in the inferior borders of the diaphragm. Thus, all the initial directions of the fibres of the diaphragmatic muscle are approximated by this radial pattern. In each element of the mesh of the diaphragm a direction is calculated according to this procedure.

The direction of the muscle fibres was determined as follows. A routine in Fortran was implemented to calculate all the directions. This routine consists of a loop that iterate among all the elements of the muscle. In each element the corresponding direction is determined. A virtual point is created outside the diaphragmatic model, sufficiently above the middle of the phrenic centre so that the whole model of the diaphragm is vertically under this point. This point is one of the two points defining the direction vector ($\underline{v}$). This vector is calculated, for each element, by a normalized projection of the difference between the coordinates of the virtual point and of the corresponding integration point. The projection of vector $\underline{v}$ in the plane $A$ of each element is given

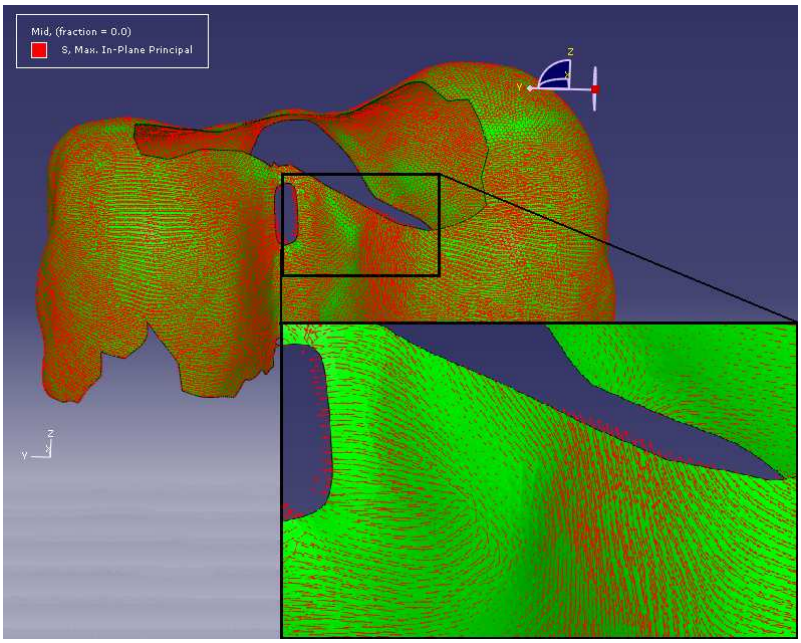


Figure 5.10: Linear elastic analysis of the diaphragm. In the left side of the zoomed image the directions of the maximum principal Cauchy stress are mainly horizontal while in the right side the directions are mainly vertical.

by

$$proj_A(\underline{v}) = A\left(A^T A\right)^{-1} A^T \underline{v} \tag{5.1}$$

where

$$A = \left[A_1^T \vdots A_2^T\right]$$

and $A_1$ and $A_2$ are vectors defining the plane obtained by considering the coordinates of the nodes of each triangular element.

The input vector necessary for the muscle model is a 2D vector in the local coordinate system. After being normalized a last matrix multiplication is required to convert the vector obtained in (5.1) to the local coordinate system.

Figure 5.11 shows the vectors defining the directions of the fibres obtained in this manner. As shown in this figure the direction of the fibres in adjacent elements is quite similar, thus approximately describing continuous radial lines.

## 5.4 Breathing Tests

In the present study the simulation of the behaviour of the diaphragm in the respiratory cycle is performed.

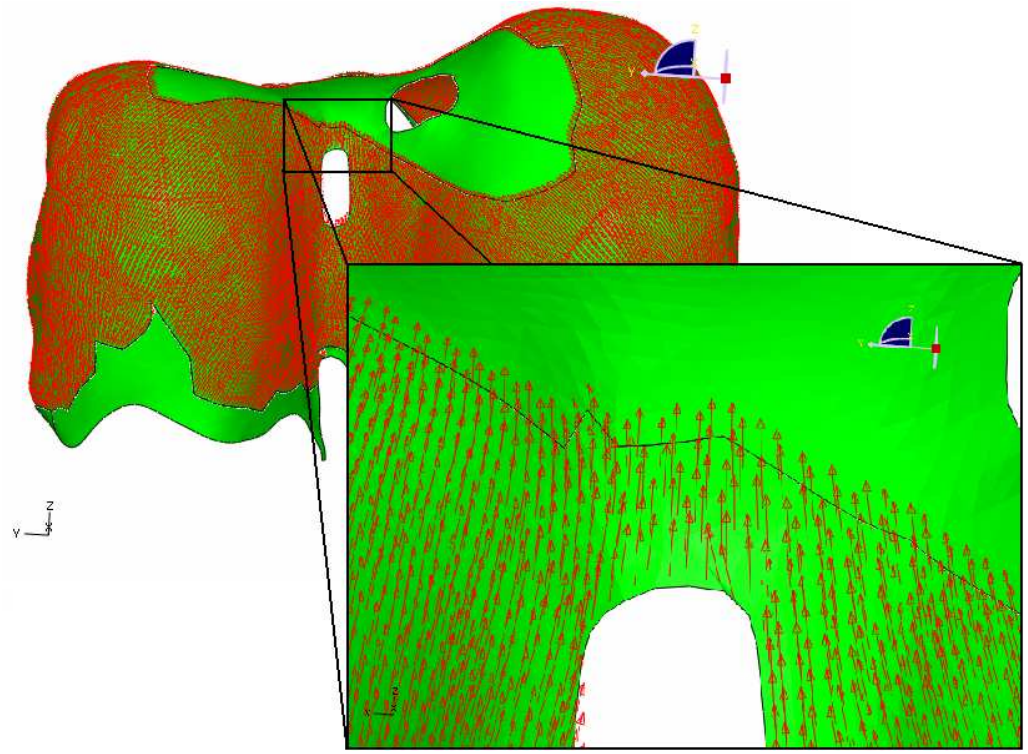

Figure 5.11: Vectors defining the direction of the fibres of the muscular tissue.

The respiratory cycle is a normal tidal breathing with a 5 seconds period with the inspiration lasting 2 seconds and the expiration lasting the remaining 3 seconds [17]. Three main analyses are performed: (i) a tidal breathing; (ii) a breathing simulating a respiratory cycle in a patient with ALS affecting the diaphragm; and finally (iii) a breathing in a patient with right hemidiaphragm paralysis derived from a complete right phrenic nerve lesion. In the normal breathing test all the fibres of the muscle of the diaphragm are active and evolve in time according to the muscle model used. On the other hand in the ALS and in the breathing with right inactivated muscle fibres, some of the fibres can not be activated. In the ALS patient the diaphragm has approximately lost 50% of the motor units, randomly distributed in the muscle. In these motor units the value of the excitation $u$ is always zero. In the second pathological analysis the right side of the diaphragm is paralysed. All motor units in the right side of the muscle become inactivated.

The value of the excitation $u_{max}$ in these analysis is not well known. Therefore various inspiration FEM analyses were performed with different values for $u_{max}$ to study the behaviour of the diaphragm for later interpretation.

### 5.4.1 Quantitative Information of the Analysis

The results obtained from the analyses provide relevant information for later interpretation and possible comparisons. There is a lot of information that can be extracted from the analyses but only some is important for the medical community. It is important to obtain the few results that can

describe and validate the analyses as much as possible.

The overall movement of the diaphragm along the respiration is well described in the medical literature. In a normal breathing the diaphragm shrinks due to the contraction of the fibres while the ribs where the diaphragm is attached expand at the same time. The domes of the diaphragm descend vertically about $1cm$ and the corresponding tidal volume is about $500cm^3$ [17].

During respiration the air enters and exits the lungs as a consequence of the movement of the diaphragm. The corresponding volume is calculated as a difference between two fictitious volumes: one obtained from the initial shape of the diaphragm and the other from its deformed configuration in a later phase of the respiration. The volume of the diaphragm at a certain instant of time is determined as follows. A virtual axial (horizontal) plane ($\pi$) is defined under the diaphragm. This plane has to be under all the elements of the diaphragm. As in the determination of the direction of the fibres, the corresponding routine has to calculate the volume in all the elements and sum the results. In each element a geometric solid similar to a triangular prism is considered but the bases of this prism are not parallel (Figure 5.12). The top base of the solid is the element of the shell (ABC in Figure 5.12) while the bottom base is defined by the projection in the virtual axial plane mentioned above of the top base.

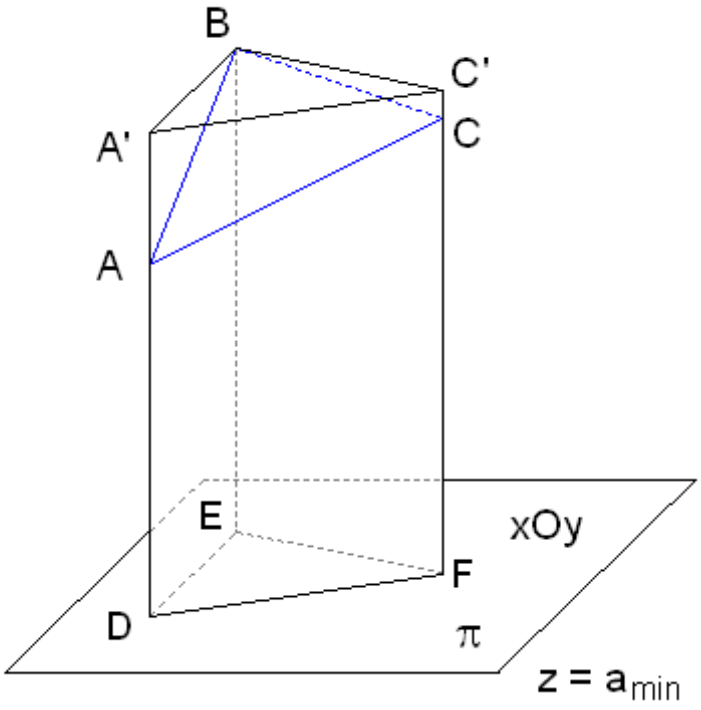


Figure 5.12: Elemental geometric solid for the volume evaluation. The element plane is the top face (ABC) of the solid.

The volume of this geometric solid ($V_{elem}$) is obtained as the difference between: (i) the volume of the regular triangular prism A'BC'DEF (Figure 5.12) where A'BC' is the projection of the shell

element ABC on the axial plane parallel to $\pi$ and containing the highest vertice (B in Figure 5.12) of the element ($V_T$); and (ii) the volume of the solid A'BC'AC ($V_{TP}$)

$$V_{elem} = V_T - V_{TP} \tag{5.2}$$

The volume $V_T$ is the volume of a regular prism

$$V_T = (M - a_{min}) \times A_B \tag{5.3}$$

where $M$ is the maximum of the axial coordinates ($z_A$, $z_B$ and $z_C$) of the vertices $A$, $B$ and $C$ of the shell element, $a_{min}$ is the axial coordinate which defines the axial virtual plane $\pi$ and $A_B$ is the area of the base of the prism given by

$$A_B = \frac{1}{2}\sqrt{\left[det\begin{pmatrix} x_A & x_B & x_C \\ y_A & y_B & y_C \\ 1 & 1 & 1 \end{pmatrix}\right]^2 + \left[det\begin{pmatrix} y_A & y_B & y_C \\ z_A & z_B & z_C \\ 1 & 1 & 1 \end{pmatrix}\right]^2 + \left[det\begin{pmatrix} z_A & z_B & z_C \\ x_A & x_B & x_C \\ 1 & 1 & 1 \end{pmatrix}\right]^2} \tag{5.4}$$

where $x_A$ and $y_A$, $x_B$ and $y_B$, and $x_C$ and $y_C$ are the coronal and saggital coordinates of the points A, B and C of the element, respectively.

The volume $V_{TP}$ is given by

$$V_{TP} = \frac{M - z_A + M - z_B + M - z_C}{3} \times A_B. \tag{5.5}$$

The volume of each geometric solid $V_{elem}$ is then given as

$$V_{elem} = \left(\frac{z_A + z_B + z_C}{3} - a_{min}\right) \times A_B. \tag{5.6}$$

# 6

# Results

## Contents

In the present Chapter all the relevant results extracted from the FEM analyses are presented.

The three dimensional model of the diaphragm was reconstructed from axial images of a female cadaver from the VHP database. The obtained geometric model was medically validated and later subjected to different FEM analyses. The first analysis performed with the model is the simulation of quiet normal inspirations with different input excitation values. The main objective of these analyses is to characterize and to determine the influence of the value of $u$ in the respiration. Indeed in a quiet normal breathing the level of excitation of the diaphragm by the phrenic nerve is still unknown. In the remaining analyses the behaviour of the model in a quiet normal breathing, in a quiet breathing in a patient with ALS pathology and in a patient with a complete right phrenic nerve lesion are simulated. In these simulations the variation of the volume and the maximum displacement of the top of the diaphragm during the respiration are evaluated.

The geometric model of the diaphragm is presented in different views in Figure 6.1. This figure shows the diaphragm in a rest and supine position. It is composed of three main regions: a top region, a lateral and surrounding region and a posterior and inferior region. The former part is represented by the domes of the diaphragm where the phrenic centre is located. The right dome of the obtained diaphragm is slightly higher than the left dome. In fact the right dome is usually higher than the left dome because the liver is located under the diaphragm and predominantly in the right side of the body. The cava vein aperture is also shown in Figure 6.1(a).

The lateral and surrounding region is formed by the apposition zone and the anterior and posterior parts of the diaphragm. The anterior part was slightly smoothed because the two slips that are usually attached to the xiphoid process of the sternum were not perceptible in the medical images. However these slips are not always present [11]. Posteriorly the model of the diaphragm has a small depression zone in its middle where the oesophageal orifice is located. This aperture is approximately elliptical and is almost parallel to the coronal plane. Laterally the diaphragm is smooth and has also some depressions corresponding to the contact of the ribs with the surface of the diaphragm. The inferior zone of the diaphragm is smoothly waved, and each peek of this wave represents the different extremities that are inserted in the ribs.

The last region, located posterior and inferiorly in the diaphragm, represents the pillars and the aortic opening. The right pillar of the model is longer and wider than the left pillar. The aortic opening is located between these two pillars and slightly displaced to the left. These characteristics are also present in Netter's schematic illustration shown in Figure 2.1(a).

With this geometric model a finite element mesh was generated using Abaqus$^{TM}$ 6.7. In Figure 6.2 the corresponding mesh consisting of triangular shell elements is shown.

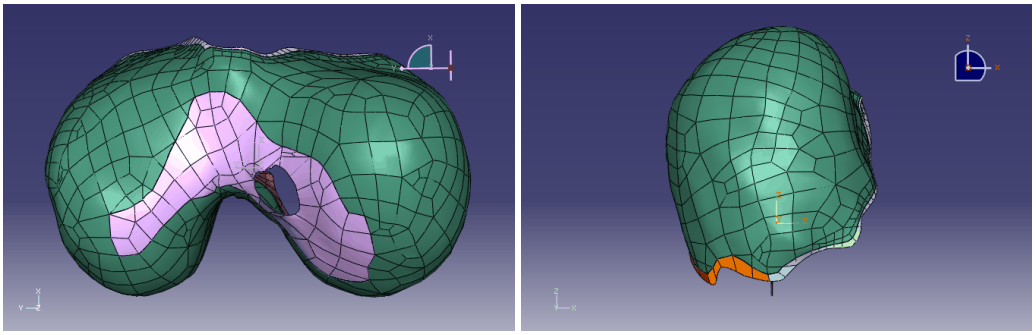

(a) (b)

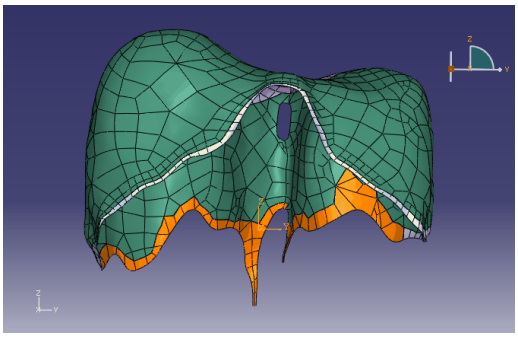

(c)

Figure 6.1: Geometric model of the diaphragm in different views: axial (a), sagittal (b) and coronal (c).

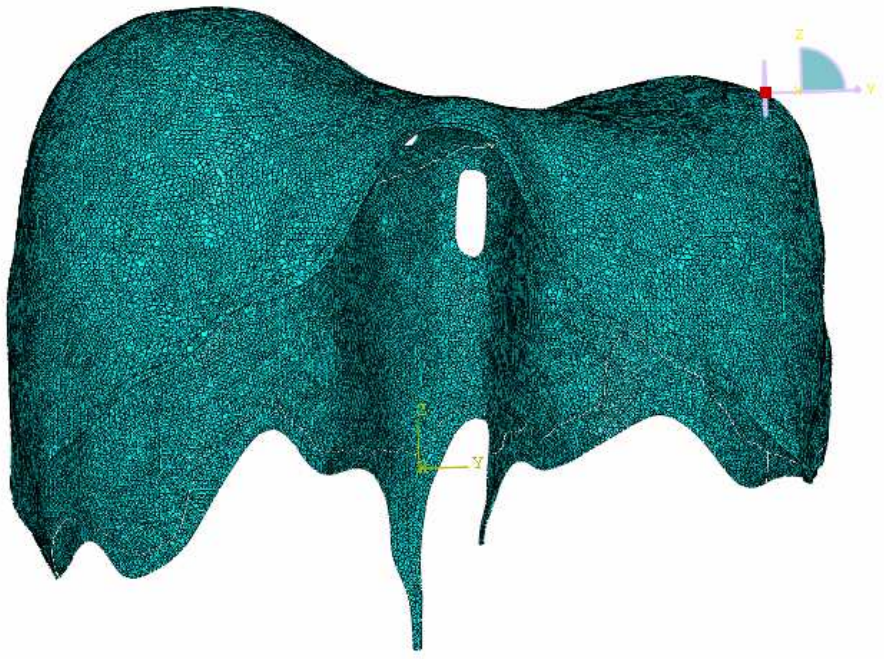

Figure 6.2: Finite element mesh of the diaphragm.

## 6.1 Variation of the neural excitation

The diaphragmatic muscle is excited from impulses originating from the respiratory centre and reaching the phrenic nerve nuclei in the cervical spinal cord. When an impulse reaches the muscle, the muscle contracts depending on the quantity of electrical energy that the fibres release into the muscle. The quantity of the excitation varies according to the desired force of the contraction. In a normal and quiet breathing the quantity of excitation released in each fibre of the diaphragm is unknown.

In the present study FEM analyses of the geometric model of the diaphragm during inspiration are performed considering different values of $u_{max}$ in the excitation function $u(t)$. The parameter values vary between 0% and 100%. When the force of contraction of the diaphragm changes not only this excitation varies. In fact the pressure under the diaphragm also changes with time during breathing and the rib cage extends when the contraction increases. Nevertheless in the current analysis the objective is only to change the value of $u_{max}$ and observe and interprete the differences.

In Table 6.1 the relevant results obtained from the analyses performed with different values of $u_{max}$ are presented. For each $u_{max}$ the tidal volume (TV) and the absolute value of the maximum axial displacement (MAD) of the top part of the diaphragm are calculated.

| $u_{max}$ (%) | Tidal Volume ($cm^3$) | Maximum Axial Displacement ($mm$) |
|---|---|---|
| 0 | 7.529 | 0.15 |
| 10 | 390.516 | 6.95 |
| 20 | 519.721 | 9.37 |
| 30 | 564.182 | 10.55 |
| 40 | 619.428 | 11.37 |
| 50 | 644.177 | 11.88 |
| 60 | 661.823 | 12.24 |
| 70 | 675.497 | 12.51 |
| 80 | 685.449 | 12.73 |
| 90 | 693.239 | 12.90 |
| 100 | 703.000 | 13.04 |

Table 6.1: Tidal volume and absolute value of the maximum axial displacement at the top of the diaphragm for different values of $u_{max}$.

The values of the tidal volume evolve approximately between 390$cm^3$ and 700$cm^3$ when the excitation of the muscle fibres is increased. The evolution of the tidal volume is not linear: for small $u_{max}$ the volume is smaller but increases rapidly, and for larger values of $u_{max}$ the tidal volume is also large but the values seem to stabilize. The evolution of the absolute value of the maximum axial displacement of the top of the diaphragmatic model is similar. Its values vary between approximately 7$mm$ and 13$mm$. When the excitation $u$ is zero the muscle fibres are not activated. Considering the small values of the volume and of the displacement at a zero excitation it is possible to conclude that the activation term in the constitutive equation is responsible for the

majority of the deformation of the diaphragm.

In a normal and quiet breathing the diaphragm does not contract at its maximum potential. In fact it is difficult to know quantitatively the percentage of the maximum contraction that occurs in a normal and quiet breathing. In the diaphragm the contraction stimulation is a complex issue because several different variables controlled mainly by the autonomous nervous system intervene and influence this process.

The values given in the literature and the results obtained for TV and MAD suggest that the best interval of $u_{max}$ to characterize the excitation in a normal quiet breathing is between 20 and 30%. It is important to stress that when the contraction of diaphragm increases, the Pdi also increases. This change was not considered in the present study. When the diaphragm is under the pressure corresponding to a quiet breathing and the excitation is high, the tidal volume and the displacement are larger than the reference values.

## 6.2 Normal Breathing

The normal quiet breathing is simulated performing a FEM analysis on the geometric model of the diaphragm during a period of 5 seconds and a value of $u_{max}$ equal to 30%. The movement of the diaphragm in a normal breathing was successfully simulated. In the inspiration the muscle of the diaphragm contracts, the domes of the diaphragm descend and its apposition and its anterior and posterior zones shrink (Figure 6.3). The decrease in the height of the domes is larger in the right dome. Indeed the obtained maximum axial displacement of the diaphragm is in the right dome region. The horizontal displacements of the lateral sides of the diaphragm as a consequence of the contraction of the muscle are smaller in comparison with the previous axial displacement of the domes. In fact the latter are approximately two to three times greater than the former. Even in the lateral side of the diaphragm the displacement to the outside is different. The posterior zone of the diaphragm has a smaller contraction in comparison with the displacement of the apposition and anterior parts of the diaphragm.

The shrinking of the diaphragm in the lateral sides is a consequence of its contraction and of the boundary conditions imposed. In a normal inspiration the diaphragm contracts to allow the domes to descend. However to guarantee the integrity of the abdominal organs, mainly the ones contacting with the diaphragm, the other respiratory muscles, the bones of the thorax and the upper part of the abdomen expand. In the present analysis the diaphragm is fixed in its boundary and then its contraction is the only relevant contribution to the horizontal displacement of the diaphragm.

In the expiration the diaphragm has a quasi-symmetric behaviour relatively to the inspiration. The domes ascend and the lateral sides of the diaphragm move to the outside. These movements characterize the relaxation of the diaphragmatic muscle.

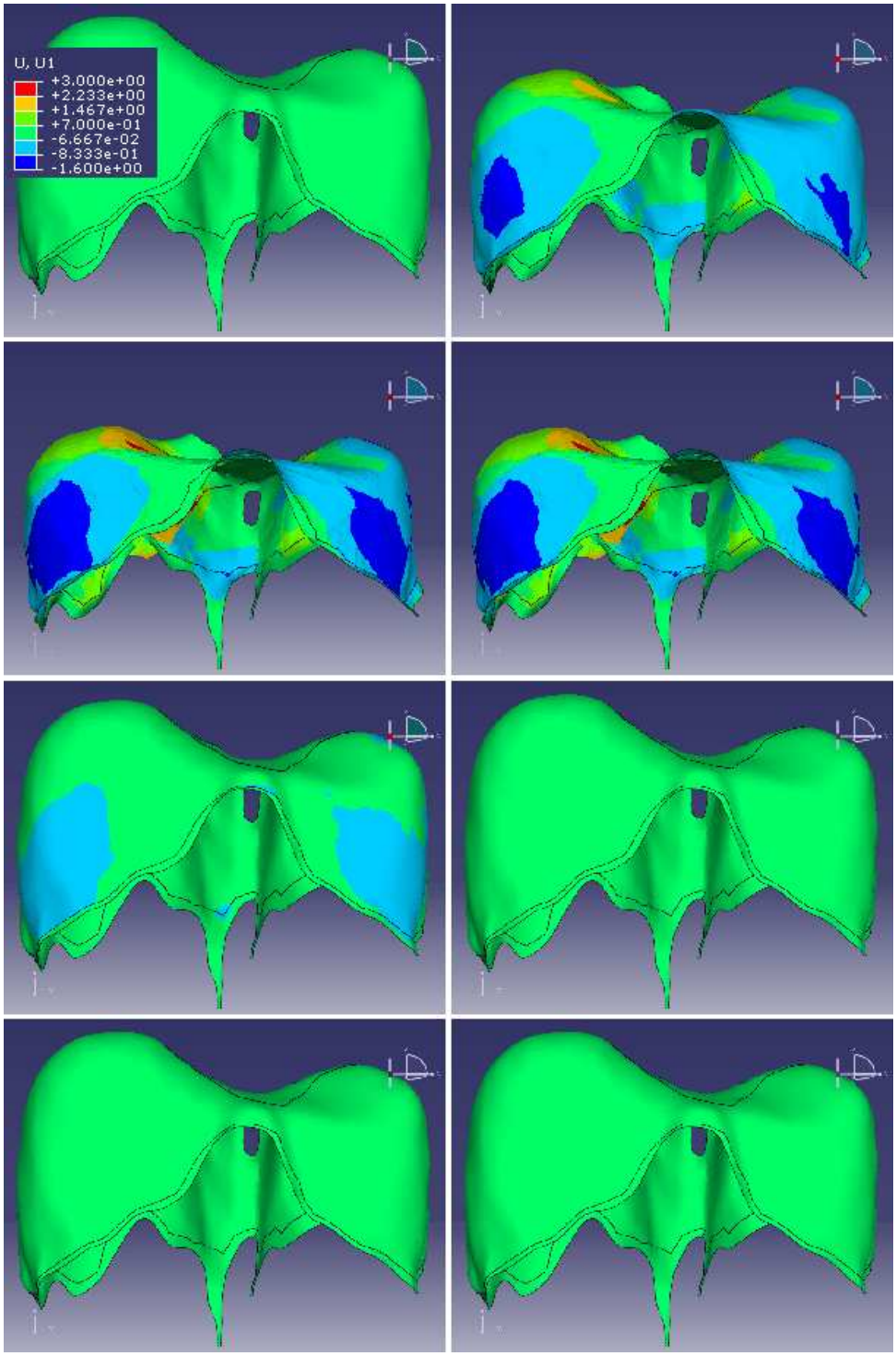


Figure 6.3: Evolution of the diaphragm in a normal quiet breathing. The model is presented in the frontal view, anterior to posterior. From top to bottom and left to right: 0, 0.5, 1, 2, 2.5, 3, 4 and 5 seconds of the respiration. The colour pattern represents the frontal displacement at each element: colours near blue in the spectrum show the displacement from posterior to anterior while the colours near red represent the opposite displacement.

The evolutions of the volume under the diaphragm and of the maximum axial displacement of the top of the diaphragm are represented in Figure 6.4.

The tidal volume is approximately 564$cm^3$ while the domes of the diaphragm descend about 10.6$mm$. The variation of the volume and of the displacement are very similar. When the diaphragm descends the volume in the lungs increases as a consequence. It is essential that these variations evolve in a similar way in order to guarantee that the variation in volume is mainly due to the descent of the domes.

Both variations have four zones during breathing. In the inspiration, all the variation in volume and displacement takes place approximately at the first second of the analysis. Similarly in the expiration, all the variation occurs approximately during the first one and a half seconds. During these periods the evolution has a quasi-exponential behaviour contrarily to the sinusoidal function considered by Segars *et al* [17] or the linear pattern obtained by Promayon *et al* [2]. At the remaining periods of time the variation is inexistent. This suggests that in a normal quiet breathing the time duration is probably smaller because the diaphragmatic muscle, in inspiration, and the expiratory muscles, in expiration, require a shorter period of time to contract. On the other hand the periods of time in inspiration and expiration when there is no variation may represent periods of gas exchange in the lungs or of muscle relaxation.

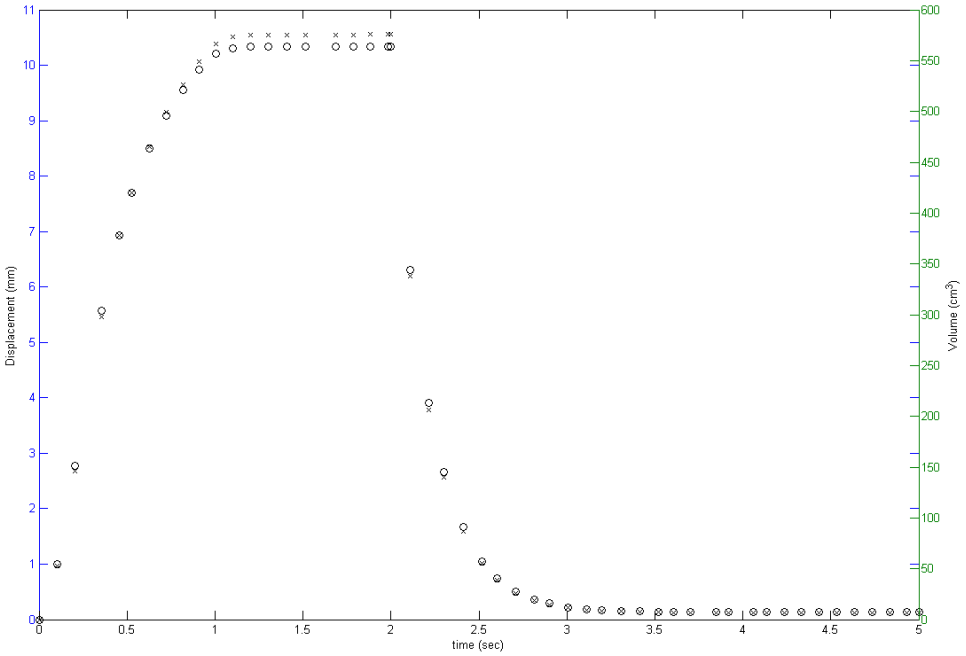


Figure 6.4: Variation of the volume ($\circ$) and of the maximum axial displacement ($\times$) of the diaphragm during a normal respiration.

The maximum-in-plane stress values vary along the surface of the diaphragm. The values of

this stress in the muscle and in the tendon are different: the stress is greater in the tendinous regions. The values of the stress in the muscle are approximately two times smaller than in some regions in the phrenic centre and in the inferior tendon. The tendon is a more rigid tissue (with larger Young's modulus) than the muscle and this is the main reason for this difference.

The maximum-in-plane stress in the muscle is approximately constant at each instant of time, with a value of 0.5309$MPa$ at the end of inspiration (see Figure 6.9(a)). On the other hand, in the majority of the tendon the maximum-in-plane stress ranges approximately between $-0.2MPa$ and $2MPa$, also at the end of inspiration. Values outside this range were located on the regions where the tendon contacts the muscle (zone of transition). These regions are mainly located (1) at the anterior part of the *inferior tendon* ($>3MPa$), (2) above the right pillar and on the posterior part of the *inferior tendon* ($< -0.5MPa$), and (3) laterally ($< -0.5MPa$).

In the muscle the directions of the maximum-in-plane stress are mainly the same as the initial orientation of the muscle fibres probably because the fibre component on the stress tensor is greater than the other contributions. Additionally there are two zones where the orientation of the stresses forms a spiral and they are located in the posterior and apposition area, but in both distal (relative to the sagittal midplane) sides of the muscle. In the tendon the orientation of the maximum-in-plane stress is less organized but in the regions where the tendon contacts the muscle, the orientation of this stress is approximately the same as in the muscle.

## 6.3 Pathological Breathings

In the present study the simulation of the respiration in a diaphragm with two pathological conditions is also performed. In both conditions about 50% of the motor units are lost. The pathological conditions considered are: a diaphragmatic dysfunction due to a ALS disease, in which the loss of motor units is random; and an unilateral inactivation of the diaphragm because of a complete lesion of one phrenic nerve. In ALS there is a parallel involvement of other muscles. Although laboratorial evaluation detects early respiratory involvement in ALS, the clinical respiratory failure is observed at later stages over the course of the disease. In a patient with a complete lesion of one phrenic nerve the paralysis occurs unilaterally in the diaphragm.

The two FEM analyses performed in the diaphragm model with the two pathological conditions were successfully simulated. The difference between these two cases and the normal quiet breathing is the inactivation of relevant elements (fibres) in the pathological diaphragm. In the analysis performed in a patient with a respiratory dysfunction due to a ALS disease the diaphragm behaviour during breathing is very similar to the evolution of the diaphragm in a normal respiration (Figure 6.5). During inspiration, both domes of the diaphragm descend axially and the lateral parts of the diaphragm shrink as a result of the contraction of the healthy fibres of the muscle. However these variations in the anatomy of the diaphragm are less significant than in the normal

diaphragm due to the presence of inactivated fibres in the muscle.

In the simulation performed under a right hemidiaphragm paralysis, during inspiration, the diaphragm contracts only in its left side and for this reason the left hemidiaphragm suffers a larger deflection comparatively to the right side (Figure 6.6). The healthy side contracts normally and this hemidiaphragm shrinks like in normal breathing. The left dome descends and the left lateral part also moves to the inside. The right paralysed hemidiaphragm suffers a small axial displacement. The right lateral part does not shrink as much as the left side and the domes descend less than in the non-pathological case.

In expiration the movement of the diaphragm in the both pathological cases is symmetric relatively to the inspiration, like in the normal breathing. In both cases the behaviour and performance of the diaphragm suffered differences during the respiration, although in the case of the right inactivated hemidiaphragm the differences are more significant. In a ALS patient the fibres of the muscle are randomly affected and inactivated while in the other lesion the inactivation is unilateral. This is the main reason for the differences in the anatomical changes in the diaphragm during breathing.

The results obtained for both the variation of the volume and for the maximum axial displacement of the diaphragm are shown in Figures 6.7 and 6.8. The evolution of both volume and displacement in both cases is similar to the evolution of the normal breathing. In the healthy fibres the contraction is normal and their behaviour remains unchanged. The main difference in the volume and displacement profiles is their values. In fact the values of the tidal volume decrease significantly in both cases. In the ALS patient the volume is approximately 306$cm^3$ (54.3% of the value of the non-pathological case) while in the right inactivated hemidiaphragm case the volume is about 196$cm^3$ (34.8% of the value of the normal case). Similarly the values of the displacement also decrease significantly. In the ALS case the maximum descent of the domes is about 5.55$mm$ (52.6% of the value of the normal case) while in the right inactivated hemidiaphragm case the descent is approximately 5.74$mm$ (54.4% of the value of the normal case). It is important to stress that the location of the points with larger values of displacement changes from the right to the left dome in the latter case due to the inactivation of the right side of the diaphragm.

The tidal volume in both cases is smaller than in the normal breathing case as expected. Nevertheless the volume of the ALS case is approximately 110$cm^3$ larger than the case of a right inactivated hemidiaphragm. It is known that the effect of the inactivation of the fibres in one of the hemidiaphragms is not significant in the performance of the quiet breathing. However the small amount of volume exchanged during the breathing indicates that the lungs are not being well ventilated. This suggests that in the case of an inactivated hemidiaphragm due to a lesion of the right phrenic nerve, there is an active compensation from the other inspiratory muscles or even from a reinforcement of the healthy fibres of the diaphragm.

In a ALS patient the dysfunction of the respiration is associated not only with the diaphragm

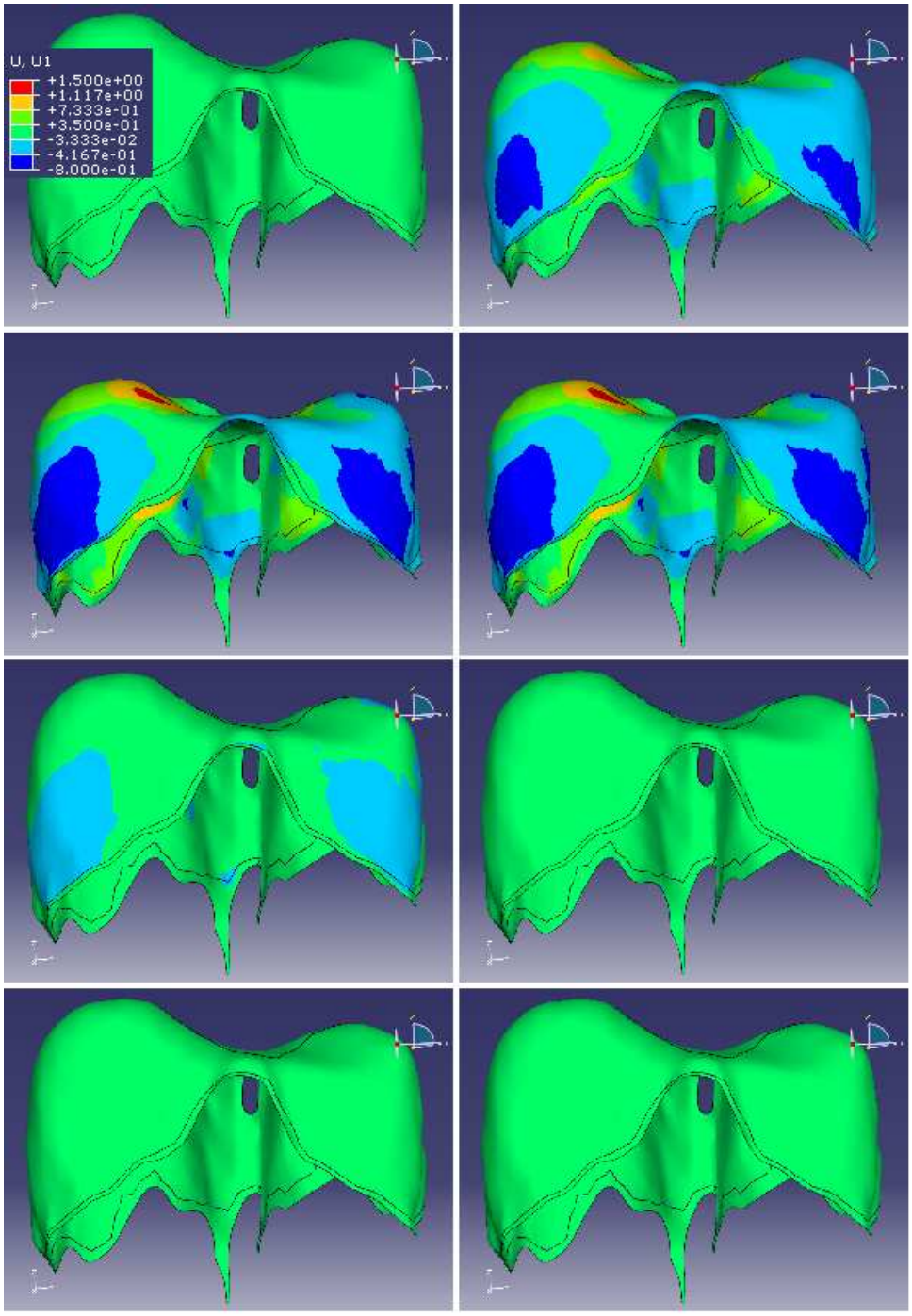


Figure 6.5: Evolution of a weak diaphragm in a quiet breathing caused by the ALS disease. The model is presented in the frontal view, anterior to posterior. From top to bottom and left to right: 0, 0.5, 1, 2, 2.5, 3, 4 and 5 seconds of the respiration. The colour pattern represents the frontal displacement at each element: colours near blue in the spectrum show the displacement from posterior to anterior while the colours near red represent the opposite displacement.

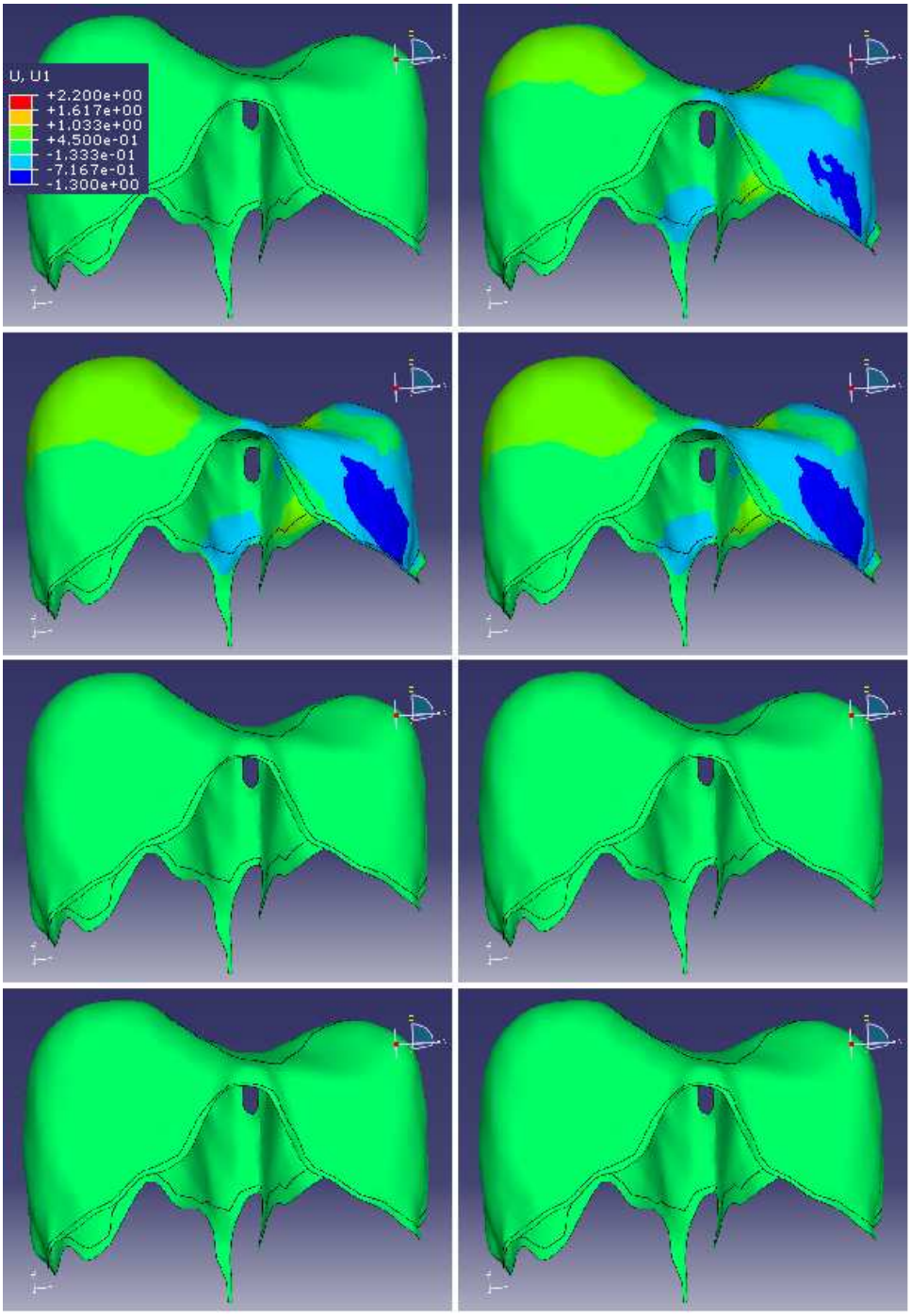


Figure 6.6: Evolution of a right inactivated diaphragm in a quiet breathing. The model is presented in the frontal view, anterior to posterior. From top to bottom and left to right: 0, 0.5, 1, 2, 2.5, 3, 4 and 5 seconds of the respiration. The colour pattern represents the frontal displacement at each element: colours near blue in the spectrum show the displacement from posterior to anterior while the colours near red represent the opposite displacement.

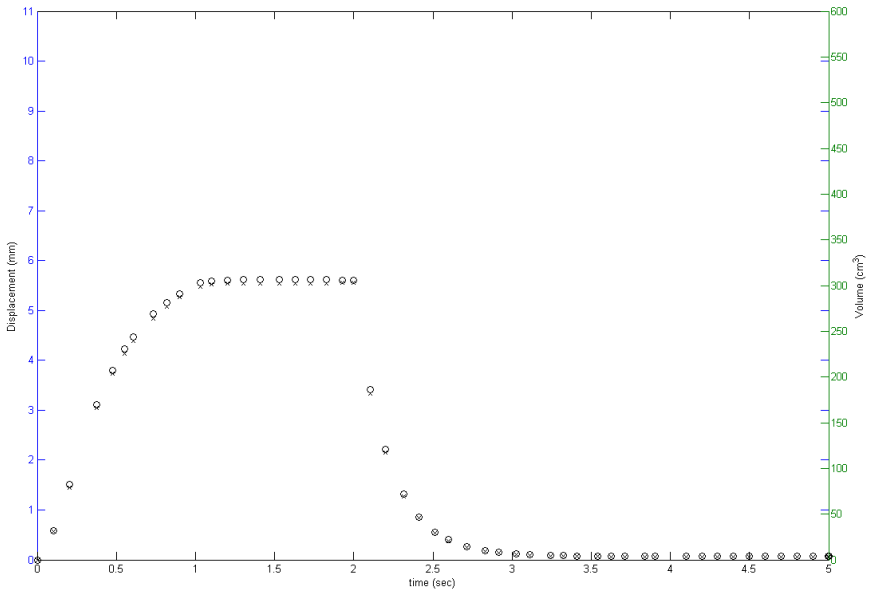


Figure 6.7: Variation of the volume (○) and maximum axial displacement (×) of the diaphragm during the respiration in a patient with respiratory dysfunction due to the ALS disease.

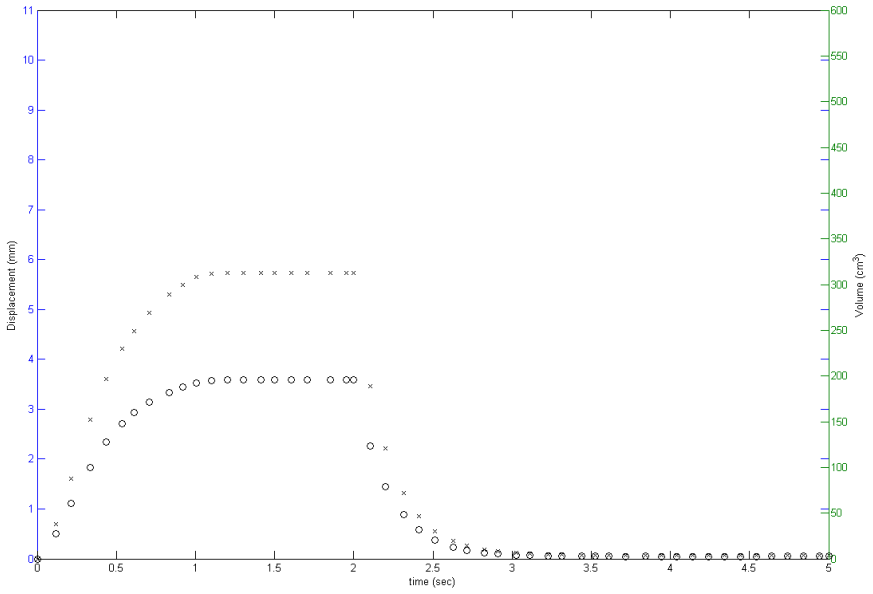


Figure 6.8: Variation of the volume (○) and maximum axial displacement (×) of an unilateral inactivated diaphragm during the respiration.

weakness but also with the involvement of other muscles. The weakness of other respiratory muscles prevents a possible compensation by the contraction of those muscles. In the case of the complete lesion of a single phrenic nerve, only one hemidiaphragm is affected. This allows the possibility for the remaining hemidiaphragm and other respiratory muscles to compensate by increasing the contraction. These results seem to suggest that a loss of motor units in the diaphragm greater than 50% is required for ALS patients to manifest symptoms of respiratory impairment.

The value of the maximum axial displacement of the diaphragm is similar in both cases and smaller than in the healthy case. However the location of the points where the axial displacement is maximum is different. In the ALS case it is located in the right dome as in the normal diaphragm, while in the other case it is located somewhere in the left dome of the diaphragm. This change is due to a decrease of the axial displacement of the elements of the right dome because of the inactivation of the right hemidiaphragm.

In the pathological cases the distribution of the values of the maximum-in-plane stress are similar in comparison with the normal case (see Figure 6.9, (b) and (c)). In the muscle, at the end of inspiration, the value of the stresses in the activated fibres is also 0.5309$MPa$ while in the inactivated fibres the value is very small, $\sim$10$^{-7}$. In the muscle the orientation of the maximum-in-plane stress is similar to the normal case. In the case of the right inactivated hemidiaphragm, however, the profile of the stress is not present in the right side of the diaphragm due to its small value. Therefore the spiral orientation of the stresses in the right side of the muscle was not identified.

In the majority of the tendon the values of the maximum-in-plane stress vary between $-$0.1$MPa$ and 1$MPa$, at the end of inspiration, in both pathological cases. These values are smaller than in the normal case. The maximum and minimum values of this stress are generally in the same regions that were identified in the normal case. In the case of the right inactivated hemidiaphragm, however, the values of this stress in the lateral side of the *inferior tendon* are significantly smaller in comparison with the normal and the ALS cases. The orientation of the maximum-in-plane stress in both pathological cases is generally more chaotic in comparison with the normal case. In the zone of transition, values greater than 1$MPa$ were obtained and the orientation of this stress does not follow the direction of the same stress in the muscle.

The boundary of the model of the diaphragm was considered fixed in displacement. When the borders are fixed the simulation of the movement of the ribs is not present. Consequently the variation of the volume at the lateral sides of the diaphragm is different. In the inspiration the movement of the ribs to the outside induces a small lateral expansion of the diaphragm although there is contraction of this organ. In this case the variation of the volume in those regions is negative which means that the volume in the lungs decreases. Without the movement of the

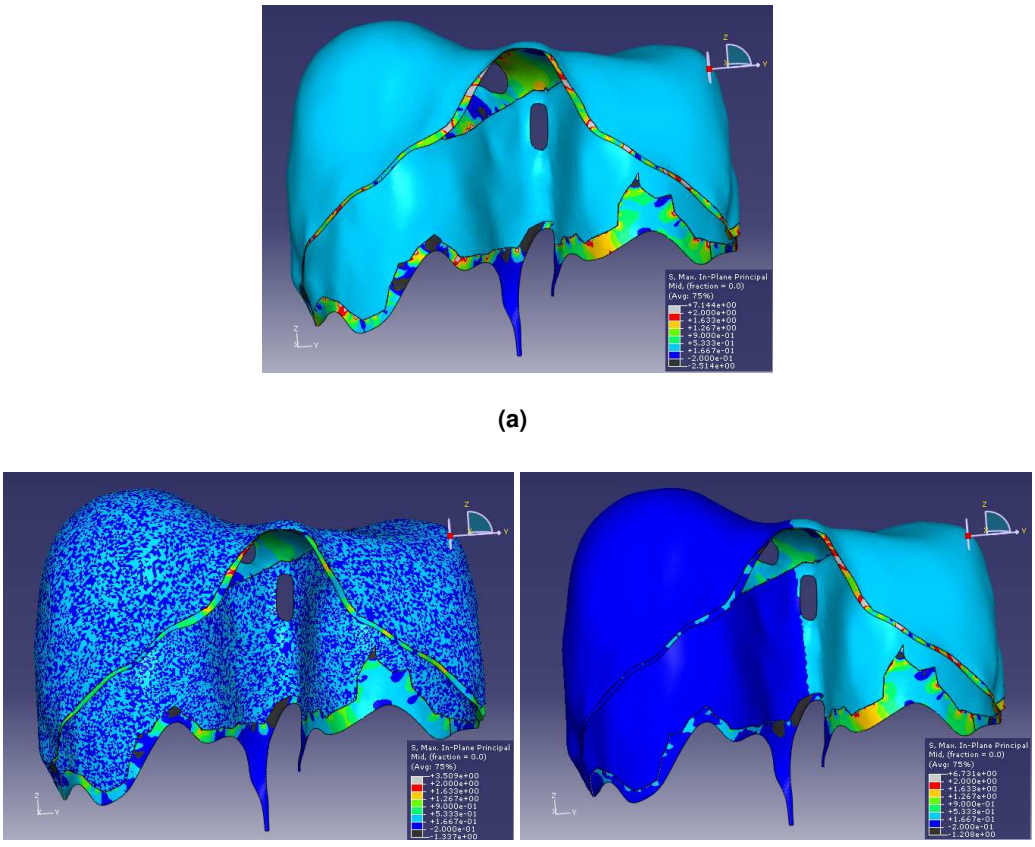

(a)

(b) (c)

Figure 6.9: Maximum-in-plane principal stress profile, at the end of inspiration, in normal (a), ALS (b) and right inactivated hemidiaphragm (c) cases.

ribs, the lateral parts of the diaphragm shrink, the variation of the volume in the same regions is positive, and the volume in the lungs increases. In consequence it is possible that the variation of the volume obtained in the FEM analysis is overestimated. These overestimations are not significant in view of the fact that the sagittal and coronal displacements of the lateral sides of the diaphragm are small comparatively to the displacements of the axial direction.

# 7

# Conclusions and Future Developments

In this thesis, computational simulations of the mechanical behaviour of the diaphragm in healthy and pathological conditions were performed. First a three-dimensional geometric model of the diaphragm obtained from medical images taken from a cadaver was constructed. A constitutive model for 3D skeletal muscles that incorporates both passive and active behaviours was adopted. A finite element mesh with triangular S3 shell elements was generated and the muscle behaviour was incorporated in Abaqus™ package by implementing a UMAT subroutine. After providing the data relative to the material properties of the tissues involved, imposing boundary and initial conditions and applying a pressure in the outer surface of the diaphragm, several numerical simulations were performed. A parametric study of the constant value of the neural excitation to be applied during inspiration was carried out. Results for the tidal volume, the maximum axial displacement of the diaphragm and for the stresses were obtained in healthy and pathological conditions during quiet breathing. The pathological conditions considered correspond to patients with a diaphragmatic dysfunction due to amyotrophic lateral sclerosis and with a right inactivated hemidiaphragm caused by a unilateral lesion of the phrenic nerve.

The reconstruction of the diaphragm required manual procedures. The diaphragm was reconstructed from photographic axial sectional images of the thoracic and abdominal contents of a female specimen obtained from the Visible Human Project.

Two different types of tissue were considered in the diaphragm: tendon and muscle. These two tissues were identified and assigned to both the geometric and the finite element model. The tendon was assumed to be linear elastic and isotropic. The skeletal muscle has contractile and active properties that require a complex model for its characterization. In the present work, a modified form of the incompressible transversely isotropic hyperelastic model proposed earlier by Humphrey & Yin [26] for the cardiac muscle was adopted. This modified model follows previous works [7][27] and incorporates both passive and active behaviours.

Some of the functions of the diaphragm that do not have an important role in the respiration were discarded. For instance, the function of the diaphragm in swallowing and emesis which is fulfilled by the crural diaphragm [12] was not considered in this study.

In the finite element simulations the diaphragm was considered fixed in displacement at the inferior borders. The axial displacement of the borders of the cava vein and oesophageal apertures and of the aortic opening was kept free while their coronal and sagittal displacements were fixed. Also rotational constraints were imposed at some regions in the inferior borders of the diaphragm. In order to apply two different constant pressures, the diaphragm was subdivided in two different regions.

Numerical simulations were performed with different values of the constant neural excitation, $u_{max}$, to be applied during inspiration. The objective of these simulations was to obtain an estimation of $u_{max}$ to be used in subsequent analyses.

The model of the diaphragm considered in the present study was then submitted to three dif-

ferent FEM analyses. The first case considered corresponds to a normal and quiet breathing five seconds long. The remaining two analyses simulate diaphragmatic dysfunctions caused by two distinct diseases. In one situation random fibres of the muscle of the diaphragm are denervated and inactive, as a consequence of ALS. In the second pathological case the fibres of the muscle of the diaphragm are also denervated but only on the right hemidiaphragm. This denervation is caused by a complete right phrenic nerve lesion.

Results for the above mentioned finite element analyses were obtained and presented. The most relevant results consist of the variation of the volume between the current and the initial configurations and of the maximum axial displacement of the diaphragm. These results allow the characterization of the evolution of the diaphragm during breathing. Additionally, sequential images of the diaphragm at different instants of time during the respiration were presented.

In the simulations regarding the excitation function, both volume and displacement showed identical evolution as a function of $u_{max}$. For small values of $u_{max}$ ($<$10%) both volume and displacement are also small. They evolve approximately as an exponential function and for larger values of $u_{max}$ they do not change significantly. In the normal quiet breathing a tidal volume of approximately 564$cm^3$ and a maximum axial displacement of the right dome of about 10.6$mm$ were obtained. The variation of these two quatities with time have a similar evolution. The evolution of these quantities has also a similar pattern in the two pathological cases. The evolution of the volume and of the displacement have a quasi-exponential behaviour in both inspiration and expiration.

The results in the analyses of the pathological cases showed that in both cases the tidal volume and the maximum axial displacement of the diaphragm decrease significantly in comparison to the normal breathing case. The values of the maximum axial displacement in both cases are identical but its location in the diaphragm is different: in the case of a complete right phrenic nerve lesion it is located on the left dome while in the ALS it is located on the right dome. The reduction of the tidal volume in the inactivated hemidiaphragm case is larger than in the ALS affected diaphragm. This last result suggests that, in view of medical knowledge retrieved from clinical cases, the diaphragm and/or other inspiratory muscles produce a compensation response in the case of inactivation of a hemidiaphragm.

In the present thesis a female specimen of the VHP was considered for the reconstruction of the diaphragm. As a future development, it is proposed that the reconstruction of the diaphragm of the male cadaver should also be performed. In the VHP the male specimen is significantly younger than the female donor considered in this work. Additionally, the diaphragm can present significant anatomical differences in view of the gender.

The diaphragm has a movement relative to the body as a consequence of the movement of the other inspiratory muscles and ribs. A more accurate analysis should be considered by allowing

the borders of the diaphragm during respiration to displace. The values of the displacement of the inferior borders of the diaphragm may be determined from medical imaging of a quiet breathing or obtained from the literature. It is important to refer that in this case the volume has to be differently determined. Indeed the procedure used in this work to calculate the volume is based on the fact that the diaphragm is fixed in a closed curve at all times.

It would also be important to consider different and eventually more regions to apply the pressure. This requires a more detailed description of the Pdi on the surface of the diaphragm.

# Bibliography


[1] F. H. Netter, “Atlas interativo de anatomia humana,” Software, Novartis Medical Education, 1999.

[2] E. Promayon and L. Gaillard, “Modèle fonctionnel du diaphragme pour l’acquisition et le diagnostic en imagerie médicale,” Tech. Rep., 2002/2003.

[3] D. C. Poole, W. L. Sexton, G. A. Farkas, S. K. Powers, and M. B. Reid, “Diaphragm structure and function in health and disease,” Medicine & Science in Sports & Exercise, vol. 29, no. 6, pp. 738–54, January 1997.

[4] A. Condurache, T. Aach, K. Eck, J. Bredno, and T. Stehle, “Fast and robust diaphragm detection and tracking in cardiac x-ray projection images,” Proceedings of the SPIE, vol. 5747, pp. 1766–75, 2005.

[5] M. Quaranta, C. Salito, E. Magalotti, P. Monaco, C. Forlani, A. Pedotti, and A. Aliverti, “Non-invasive three-dimensional imaging of human diaphragm in-vivo,” Engennering in Medicine and Biology Society, pp. 5278–81, August 2008.

[6] A. C. Guyton and J. E. Hall. Guanabara Koogan, 2002, ch. Contracção do Músculo Esquelético, pp. 63–74.

[7] J. A. C. Martins, M. P. M. Pato, and E. B. Pires, “A finite element model of skeletal muscles,” Virtual and Physical Prototyping, vol. 1, no. 3, pp. 159–70, September 2006.

[8] M. J. Ackerman, “The visible human project,” Proceedings of the IEEE, vol. 86, no. 3, pp. 504–11, March 1998.

[9] A. Ratnovsky and D. Elad, “Anatomical model of the human trunk for analysis of respiratory muscles mechanics,” Respiratory Physiology & Neurobiology, no. 148, pp. 245–62, 2005.

[10] N. Lechtzin, “Respiratory effects of amyotrophic lateral sclerosis: Problems and solutions,” Respiratory Care, vol. 51, no. 8, pp. 871–81, August 2006.

[11] G. R. Harrison. Springer London, 2005, ch. The Anatomy and Physiology of the Diaphragm, pp. 45–58.

[12] M. Pickering and J. F. X. Jones, “The diaphragm: two physiological muscles in one,” J. Anat., no. 201, pp. 305–12, July 2002.

[13] A. M. Boriek, N. G. Kelly, J. R. Rodarte, and T. A. Wilson, “Biaxial constitutive relations for the passive canine diaphragm,” J Appl Physiol, no. 89, pp. 2187–90, July 2000.

[14] F. Dangond, “Amyotrophic lateral sclerosis,” Online Article, emedicine - WebMD, April 2006. [Online]. Available: http://emedicine.medscape.com/article/1170097-overview

[15] W. Robberecht, L. Van Den Bosch, and V. Vleminckx, “Amyotrophic lateral sclerosis: Pathogenesis,” Acta neurol. belg., no. 100, pp. 181–7, 2000.

[16] M. Behr, L. Thollon, P.-J. Arnoux, T. Serre, S. V. Berdah, P. Baque, and C. Brunet, “3d reconstruction of the diaphragm for virtual traumatology,” Surg Radiol Anat, no. 28, pp. 235–40, February 2006.

[17] W. P. Segars, D. S. Lalush, and B. M. Tsui, “Modeling respiratory mechanics in the mcat and spline-based mcat phantoms,” IEEE Transactions on Nuclear Science, vol. 48, no. 1, pp. 89–97, February 2001.

[18] V. Spitzer, M. J. Ackerman, A. Scherzinger, and D. Whitlock, “The visible human male: A technical report,” J. Amer. Med. Informatics Assoc., vol. 3, no. 2, pp. 118–30, 1996.

[19] L. Zheng, L. Rico, R. Lasher, and A. Vasavada, “Biomechanical neck model based on the visible human female,” Conference of American Society of Biomechanics at Palo Alto, CA, no. 31, 2007.

[20] L. Hoyte, L. Schierlitz, K. Zou, G. Flesh, and J. R. Fielding, “Two- and 3-dimensional mri comparison of levator ani structure, volume, and integrity in women with stress incontinence and prolapse,” American Journal of Obstetrics and Gynecology, vol. 185, no. 1, pp. 11–9, July 2001.

[21] W. E. Lorensen and H. E. Cline, “Marching cubes: A high resolution 3d surface construction algorithm,” Computer Graphics, vol. 21, no. 4, pp. 163–9, July 1987.

[22] E. Promayon, “Modèle et simulation de la repiration,” Ph.D. dissertation, Université Joseph Fourier, Grenoble, 1997.

[23] D. D’Aulignac, J. A. C. Martins, E. B. Pires, T. Mascarenhas, and R. M. N. Jorge, “A shell finite element model of the pelvic floor muscles,” Computer Methods in Biomechanics and Biomedical Engineering, vol. 8, no. 5, pp. 339–47, October 2005.

[24] J. A. C. Martins, E. B. Pires, R. Salvado, and P. B. Dinis, “A numerical model of passive and active behaviour of skeletal muscles,” Computer Methods in Applied Mechanics and Engineering, no. 151, pp. 419–33, 1998.

[25] D. d'Aulignac, J. A. C. Martins, and E. B. Pires, "Physical modeling of the pelvic floor muscles using shell elements," European Congress on Computational Methods in Applied Sciences and Engineering, July 2004.

[26] J. D. Humphrey and F. C. P. Yin, "On constitutive relations and finite deformations of passive cardiac tissue: I. a pseudostrain-energy function," ASME Journal of Biomechanical Engineering, no. 109, pp. 298–304, 1987.

[27] J. A. C. Martins, M. P. M. Pato, E. B. Pires, R. M. N. Jorge, M. Parente, and T. Mascarenhas, "Finite element studies of the deformation of the pelvic floor," Annals of the New York Academy of Sciences, vol. 1101, pp. 316–34, 2007.

[28] M. P. M. Pato and P. M. A. Areias, "Active and passive behavior of soft tissues: pelvic floor muscles," Communications in Numerical Methods in Engineering, 2009, (Accepted).

[29] A. P. Santhanam, C. M. Fidopiastis, F. G. Hamza-Lup, J. P. Rolland, and C. Imielinska, "Physically-based deformation of high-resolution 3d lung models for augmented reality based medical visualization," Medical Image Computing and Computer-Assisted Intervention Conference, Augmented environments for Medical Imaging-Augmented Reality in Computer-aided Surgery Workshop at Rennes, France, pp. 21–32, September 2004.

[30] T. Similowski, V. Attali, G. Bensimon, F. Salachas, S. Mehiri, I. Arnulf, L. Lacomblez, M. Zelter, V. Meininger, and J.-P. Derenne, "Diaphragmatic dysfunction and dyspnoea in amyotrophic lateral sclerosis," Eur Respir Journal, no. 15, pp. 332–7, 2000.

[31] P. L. Schiffman and J. M. Belsh, "Pulmonary function at diagnosis of amyotrophic lateral sclerosis. rate of deterioration." CHEST, vol. 166, no. 103, pp. 508–13, 1993.

[32] H. Stewart, A. Eisen, J. Road, M. Mezei, and M. Weber, "Electromyography of respiratory muscles in amyotrophic lateral sclerosis," Journal of the Neurological Sciences, vol. 191, pp. 67–73, 2001.

[33] A. Jubran, "Critical illness and mechanical ventilation: Effects on the diaphragm," Respiratory Care, vol. 51, no. 9, pp. 1054–64, September 2006.

[34] I. Arnulf, T. Similowski, F. Salachas, L. Garma, S. Mehiri, V. Attali, V. Behin-Bellhesen, V. Meininger, and J.-P. Derenne, "Sleep disorders and diaphragmatic function in patients with amyotrophic lateral sclerosis," Am J Respir Crit Care Med, vol. 161, pp. 849–56, 2000.

[35] C. Shindoh, W. Hida, H. Kurosawa, S. Ebihara, Y. Kikuchi, T. Takishima, and K. Shirato, "Effects of unilateral phrenic nerve denervation on diaphragm contractility in rat," Tohoku J. Exp. Med., vol. 173, pp. 291–302, 1994.

[36] J.-P. Marie, C. Tardif, Y. Lerosey, J. Gibon, M. Hellot, M. Tadié, J. Andrieu-Guitrancourt, D. Dehesdin, and P. Pasquis, "Selective resection of the phrenic nerve roots in rabbits. part ii: Respiratory effects," Respiration Physiology, vol. 109, pp. 139–48, 1997.

[37] J.-P. Marie, Y. Lacoume, A. Laquerrière, C. Tardif, J. Fallu, G. Bonmarchand, and E. Verin, "Diaphragmatic effects of selective resection of the upper phrenic nerve root in dogs," Respiratory Physiology & Neurobiology, vol. 154, pp. 419–30, 2006.

[38] C. M. Laroche, A. K. Mier, J. Moxham, and M. Green, "Diaphragm strength in patients with recent hemidiaphragm paralysis," Thorax, vol. 43, pp. 170–4, 1988.

[39] J. M. Winters, "Hill model: Contractile element in series and parallel with elastic elements," Online Article, Marquette University, 2004. [Online]. Available: http://www.eng.mu.edu/wintersj/muscmod/musc-modeling/musc-struc/ce-se.htm

[40] A. Ratnovsky, U. Zaretsky, R. J. Shiner, and D. Elad, "Integrated approach for in vivo evaluation of repiratory muscles mechanics," Journal of Biomechanics, no. 36, pp. 1771–84, May 2003.

[41] M. G. Pandy, F. E. Zajac, E. Sim, and W. S. Levine, "An optimal control model for maximum-height human jumping," Journal of Biomechanics, vol. 12, no. 23, pp. 1185–98, 1990.

[42] A. P. Grieve and C. G. Armstrong. Free University Press, 1988, ch. Compressive properties of soft tissues, pp. 531–6.

[43] D. S. Lopes, J. A. Martins, and E. B. Pires, "Three-dimensional reconstruction of biomechanical structures for finite element analysis," Poster, 2008.

[44] N. Ribeiro, P. C. Fernandes, D. S. Lopes, J. Folgado, and P. R. Fernandes, "3-d solid and finite element modeling of biomechanical structures - a software pipeline," Proceedings of the 7th EUROMECH Solid Mechanics Conference, 2009.

[45] A. M. Boriek, J. R. Rodarte, and M. B. Reid, "Shape and tension distribution of the passive rat diaphragm," Am J Physiol Regulatory Integrative Comp Physiol, vol. 280, pp. R33–R41, 2001.

[46] M. J. Tobin, L. Brochard, and A. Rossi, "Assessment of respiratory muscle function in the intensive care unit," Am J Respir Crit Care Med, vol. 166, no. 10, pp. 610–23, 2002.